An approach for quantitative mapping of synaptic periactive zone architecture and organization

Steven J. Del Signore[a],*, Margalit G. Mitzner[a], Anne M. Silveira[a], Thomas G. Fai[b], and Avital A. Rodal[a],*
aDepartment of Biology and bDepartment of Mathematics, Brandeis University, Waltham, MA 02453

ABSTRACT Following exocytosis at active zones, synaptic vesicle membranes and membrane-bound proteins must be recycled. The endocytic machinery that drives this recycling accumulates in the periactive zone (PAZ), a region of the synapse adjacent to active zones, but the organization of this machinery within the PAZ, and how PAZ composition relates to active zone release properties, remains unknown. The PAZ is also enriched for cell adhesion proteins, but their function at these sites is poorly understood. Here, using Airyscan and stimulated emission depletion imaging of *Drosophila* synapses, we develop a quantitative framework describing the organization and ultrastructure of the PAZ. Different endocytic proteins localize to distinct regions of the PAZ, suggesting that subdomains are specialized for distinct biochemical activities, stages of membrane remodeling, or synaptic functions. We find that the accumulation and distribution of endocytic but not adhesion PAZ proteins correlate with the abundance of the scaffolding protein Bruchpilot at active zones—a structural correlate of release probability. These data suggest that endocytic and exocytic activities are spatially correlated. Taken together, our results identify novel relationships between the exocytic and endocytic apparatus at the synapse and provide a new conceptual framework to quantify synaptic architecture.

INTRODUCTION

Endocytic proteins fulfill multiple physiological functions at the synapse, including synaptic vesicle endocytosis and recycling, transmembrane protein trafficking, release site clearance, and cargo

sequestration (Azarnia Tehran and Maritzen, 2022). The dozens of endocytic proteins that drive these diverse functions accumulate at micromolar concentrations at synapses (Wilhelm *et al.*, 2014) and in many cases are predeployed to the plasma membrane (Del Signore *et al.*, 2021; Imoto *et al.*, 2022) in a poorly defined micron-scale domain called the periactive zone (PAZ) (Roos and Kelly, 1999; Sone *et al.*, 2000; Jiao *et al.*, 2010; Cano and Tabares, 2016). This is in sharp contrast to nonneuronal cells, where the same endocytic proteins are recruited to diffraction-limited membrane spots in a well-defined temporal sequence (Kaksonen and Roux, 2018). These unique features of endocytic proteins at synapses highlight the need to investigate the synapse-specific mechanisms that control endocytic protein recruitment and activity. However, the imaging-based approaches that have been so useful in other cell types for measuring the sequential recruitment and actions of endocytic proteins are incompatible with the high concentration and constitutive predeployment of endocytic proteins at the synapse. Thus, it remains difficult to investigate how synapses control where and when endocytic molecules are active relative to sites of exocytosis and how the recruitment and activation of dozens of endocytic proteins

are tailored to their many synaptic functions, particularly the trafficking of diverse cargoes.

Despite the high concentration of endocytic proteins at the PAZ, this region is not a monofunctional endocytic zone. Endocytosis can proceed through multiple distinct molecular mechanisms (e.g., Clathrin mediated, bulk, ultrafast, kiss-and-run) (Gan and Watanabe, 2018) and occur both within the PAZ and at/near active zones (Kosaka and Ikeda, 1983; Koenig and Ikeda, 1996; Teng and Wilkinson, 2000; Kidokoro, 2006; Kuromi *et al.*, 2010; Watanabe *et al.*, 2013a). Further, PAZ molecules have many functions beyond synaptic vesicle endocytosis, as mentioned above. Finally, in addition to endocytic proteins the PAZ contains a high concentration of synaptic adhesion molecules. Synaptic adhesion proteins regulate synapse formation, maintenance, and plasticity and are implicated in multiple neurological disorders (Jang *et al.*, 2017; Sytnyk *et al.*, 2017; Südhof, 2018). They are especially interesting to consider as PAZ constituents because they regulate endocytosis and synaptic vesicle trafficking (Leshchyns'ka *et al.*, 2006; Shetty *et al.*, 2013; van Stegen *et al.*, 2017; Dagar *et al.*, 2021; Luo *et al.*, 2021) and are themselves endocytic cargoes. Indeed, presynaptic endocytosis and trafficking pathways regulate the levels and function of adhesion molecules (Bailey *et al.*, 1992; Yamada *et al.*, 2007; Fu and Huang, 2010; Nahm *et al.*, 2016; Kurshan *et al.*, 2018; Blanchette *et al.*, 2022). Therefore, in addition to being important components of the PAZ, adhesion molecules are crucial regulators and effectors of the endocytic machinery at the synapse. Our goal in the current work is to develop an approach to quantify the distribution of endocytic and adhesion molecules at the PAZ to begin to provide insight into their different functions.

The elaborate organization of endocytic and adhesion molecules into a PAZ domain is conserved in many synapse types across species. It has been most frequently described at large synapses such as the *Drosophila* neuromuscular junction (NMJ) (Estes *et al.*, 1996; Schuster *et al.*, 1996; González-Gaitán and Jäckle, 1997; Roos and Kelly, 1999; Sone *et al.*, 2000; Wan *et al.*, 2000; Koh *et al.*, 2004; Marie *et al.*, 2004; Rodal *et al.*, 2008; Kawasaki *et al.*, 2011), photoreceptor ribbon synapses (Gray and Pease, 1971; Wahl *et al.*, 2013, 2016), and lamprey reticulospinal axons (Bloom *et al.*, 2003; Evergren *et al.*, 2004). Endocytic proteins are also predeployed adjacent to active zones at small central synapses such as in hippocampal neurons (Gerth *et al.*, 2017; Imoto *et al.*, 2022). The evidence that the PAZ is a bona fide membrane domain derives from direct observations of endocytic membrane intermediates by electron microscopy (EM) (Heuser and Reese, 1973; Watanabe *et al.*, 2013b), by the enrichment of endocytic or synaptic vesicle-associated F-actin by EM and fluorescence microscopy (Shupliakov *et al.*, 2002; Bloom *et al.*, 2003; Del Signore *et al.*, 2021), and by the accumulation of known endocytic proteins by EM and fluorescence microscopy (Sone *et al.*, 2000; Marie *et al.*, 2004; Jiao *et al.*, 2010; Kawasaki *et al.*, 2011; Gerth *et al.*, 2017; Del Signore *et al.*, 2021; Imoto *et al.*, 2022). While most studies have treated the PAZ as a homogeneous and ill-defined structure, there are hints that some PAZ components, such as the adhesion protein FasciclinII (FasII), might accumulate in distinct subdomains around the active zone (Marie *et al.*, 2004; Jiao *et al.*, 2010).

A further open question is how the spatial organization of the PAZ or other endocytic zones might be coupled to the exocytic machinery. At synapses generally, release sites are associated with active zones, which recruit and organize release machinery, synaptic vesicles, and voltage-gated calcium channels (Petzoldt *et al.*, 2016; Ghelani and Sigrist, 2018). As such, active zone composition and architecture are important determinants of synaptic physiological

and homeostatic properties (Kittel *et al.*, 2006; Fouquet *et al.*, 2009; Böhme *et al.*, 2019; Goel *et al.*, 2019; Hong *et al.*, 2020). For example, at the *Drosophila* NMJ, different active zones even within a single neuron exhibit up to 50-fold differences in release probability for both evoked and spontaneous release. These differences in release probability correlate with the age of the active zone and with the composition and organization of active zone components including Brp/CAST and voltage-gated calcium channels (Melom *et al.*, 2013; Akbergenova *et al.*, 2018; Gratz *et al.*, 2019; Newman *et al.*, 2022). However, it remains unknown whether or how active zone assembly and physiology might control PAZ properties. This includes whether and how the endocytic machinery organizes developmentally (over minutes to hours) with respect to the release probability and composition of nearby active zones and how this organization responds acutely (in seconds) to exocytosis.

Despite these data, no study to date has systematically and quantitatively analyzed the structure and molecular patterning of a PAZ or compared the properties of a PAZ with its associated exocytic machinery. This has been a challenge because the PAZ is heterogeneous in shape and size (i.e., it is not a simple isotropic bullseye around the active zone) and its dimensions approach the limits of conventional light microscopy. Here we develop a new method to analyze the complex protein architecture of the synaptic endocytosis machinery. We apply this method to analyze the distribution of a subset of endocytic and adhesion proteins at the *Drosophila* NMJ (see Table 1), including Clathrin, Dap160, Nervous Wreck, Dynamin, and FasciclinII. We chose this panel for multiple reasons: 1) These proteins are well-studied molecules known to enrich at the PAZ at this synapse. 2) Based on loss of function phenotypes, these molecules contribute to diverse synaptic functions including endocytosis, vesicle trafficking, and adhesion. 3) The endocytic molecules selected are thought to act at distinct steps during endocytosis. This synapse is well studied, has multiple active zones per synapse, has well-characterized physiological properties, and is highly amenable to superresolution imaging. Further, the wide range of release probabilities between active zones at this synapse provide a large dynamic range to compare active zone and PAZ assemblies. With this approach, we identify several new features of PAZ architecture. First, we find that distribution of different PAZ proteins is highly heterogeneous, both within and between individual PAZ units. Second, we find that the overall structure of the PAZ is only partially defined by active zone position and pattern. Third, we find that the accumulation and distribution of specific PAZ proteins significantly correlate with the concentration of the scaffold BRP (a structural correlate of release probability) in nearby active zones. Together these findings suggest new relationships between active zone and PAZ molecular organization and pave the way for new studies investigating endocytic molecular dynamics and mechanisms that couple the assembly and function of exocytic and endocytic assemblies at synapses.

RESULTS

Endocytic and adhesion proteins heterogeneously localize to the PAZ

As a model system, we used the *Drosophila* larval NMJ (Figure 1A), which consists of large (3–6-μm diameter) synaptic boutons containing multiple (10–30) active zones, allowing us to resolve the organization of PAZ molecules at synaptic membranes (see Table 1 for a summary of genes and labeling strategies and Supplemental Figure S1 and *Materials and Methods* for reagent validation). We focused our analyses on synapses at rest, where the number of spontaneous exocytic and endocytic events is approximately five per bouton per minute (Melom *et al.*, 2013; Akbergenova *et al.*, 2018; Del Signore

Protein	Mammalian homologue	Function	Labeling strategy	Key references
Clathrin	CLC	Coat protein	GFP-tagged transgene	Heerssen et al., 2008; Kasprowicz et al., 2008
Dap160	ITSN1/2	Multi-SH3 adapter	Antibody or knock-ins	Marie et al., 2004; Koh et al., 2004; Winther et al., 2013, 2015
Nervous Wreck	FCHSD1/2	F-BAR/SH3 membrane binding	Antibody or knock-in	O'Connor-Giles et al., 2008; Rodal et al., 2008, 2011; Becalska et al., 2013; Kelley et al., 2015; Stanishneva-Konovalova et al., 2016; Del Signore et al., 2021
Dynamin/Shibire	DYN1/2/3	Membrane scission	Antibody	Estes et al., 1996; Roos and Kelly et al., 1999; Dickman et al., 2006
FasciclinII	NCAM	Cell adhesion	Antibody	Schuster et al., 1996; Davis et al., 1998; Sone et al., 2000; Beck et al., 2012
Bruchpilot	ELKS/CAST	Active zone scaffold	Antibody or knock-in	Kittel et al., 2006; Wagh et al., 2006; Fouquet et al., 2009

TABLE 1: Proteins analyzed in this study.

et al., 2021). We imaged PAZ protein distribution and architecture primarily by Airyscan microscopy and confirmed results by stimulated emission depletion (STED) microscopy (see Figure 5 later in this article). As previously observed in both live and fixed samples, we observed that PAZ proteins generally form a membrane-associated mesh surrounding active zones (Figure 1B, [Roos and Kelly, 1999; Sone et al., 2000; Koh et al., 2004; Marie et al., 2004; Winther et al., 2015; Del Signore et al., 2021]). We further noted in both live (Figure 5 later in this article and Del Signore et al., 2021) and fixed preparations (Figure 1C) that the vast majority of signal localized to the plasma membrane (or a domain adjacent to the membrane within the resolution limits of our imaging), with little signal further from the membrane, where most synaptic vesicles are distributed (Denker et al., 2009). Indeed, when we examined how synaptic vesicles are distributed relative to the PAZ, we found little overlap: We labeled vesicle pools by FM dye loading and visualized Nwk live using an endogenous HaloTag knockin (Nwk[HALO]; see Materials and Methods). At the fly NMJ, synaptic vesicles fill a large fraction of the bouton, as expected based on EM (Ramachandran and Budnik, 2010), and we observed no systematic colocalization with the predominantly plasma membrane–proximal Nwk (Supplemental Figure S2A). Thus, only a small fraction of PAZ proteins is likely sequestered in vesicle pools, though this has been a popular model proposed to regulate their deployment to the plasma membrane (Bai et al., 2010; Winther et al., 2013).

We noted a surprising complexity to the distributions of individual PAZ molecules within the PAZ, with significant variation in local concentrations and a striking degree of noncolocalization of different pairs of proteins, even those that physically interact such as Dap160 and Nwk (O'Connor-Giles et al., 2008; Rodal et al., 2008; Almeida-Souza et al., 2018) (Figure 1D). Colocalization measurements over the whole NMJ artificially inflate the colocalization of PAZ molecules with one another because other large-scale spatial relationships such as shared protein localization to the plasma membrane versus cytoplasm and partitioning to the PAZ versus active zone (Supplemental Figure S2B) obscure the relationships of these proteins within the PAZ (because it is only a small fraction of the entire synapse). To properly quantify this complexity and gain insight into the architecture of the PAZ, we segmented the synapse into a set of PAZ units, where each individual PAZ unit represents a perimeter of PAZ proteins surrounding between 0 and 3 active zones (see Figure 3E later in this article). For most experiments, we segmented PAZ architecture based on the combined fluorescence

signal of two PAZ proteins and the active zone marker BRP (Figure 1C; see Materials and Methods for rationale and details). We then subdivided each PAZ unit into exocytic "core" and endocytic "mesh" regions (Figure 1E). For a subset of analyses (see Figure 3, C and D later in this article; Supplemental Figure S6) we also segmented PAZ units using individual PAZ or active zone signals. Finally, we segmented each active zone into a discrete object to quantify its size and intensity. The respective sizes of these regions are on averag: PAZ mesh $0.237 \pm 0.05 \ \mu m^2$; PAZ core $0.101 \pm 0.01 \ \mu m^2$; active zone objects $0.054 \pm 0.002 \ \mu m^2$ (see Supplemental Figure S2C for distributions), indicating that the PAZ unit is roughly two-thirds mesh and one-third core and that approximately half the core is occupied by the active zone marker BRP.

To formally test whether the PAZ is a heterogeneous structure, we first quantified the colocalization of endocytic and adhesion molecules within the composite PAZ mesh (Figure 1F). If the PAZ is a homogeneous structure, then we expect strong and consistent pairwise colocalization between PAZ proteins. Instead, we find that Pearson R values range from less than 0.2 to 0.6, indicating significant differences in where individual proteins accumulate within the PAZ. Strikingly, these weak and variable relationships were true even for pairs such as Dynamin and Dap160, two well-characterized PAZ proteins that physically interact and whose levels, localization, and activity are coupled (Roos and Kelly, 1998; Koh et al., 2004; Rodal et al., 2008; Winther et al., 2013). As a negative control, we analyzed the colocalization of PAZ proteins with the active zone marker BRP in the mesh region (Supplemental Figure S2D). Consistently for all PAZ proteins, the Pearson R to BRP was approximately zero, supporting the conclusion that even the lowest PAZ–PAZ colocalizations are above background. Together, these observations suggest a previously unappreciated complexity to the organization of the endocytic machinery at synaptic membranes.

Proteins partition differently within the PAZ

We next asked precisely where and how PAZ proteins accumulate at individual PAZ mesh sites. We considered three ways that PAZ proteins might differentially localize—radially, by partitioning differentially between mesh and core regions; laterally, by accumulating in distinct subdomains within the PAZ mesh or core; and finally the extent to which their accumulation is diffuse versus punctate (see schematic [Figure 2A] and example images [Figure 2B]). To examine radial distribution, we generated a normalized radial profile extending from the mesh to the centroid of the core for each protein
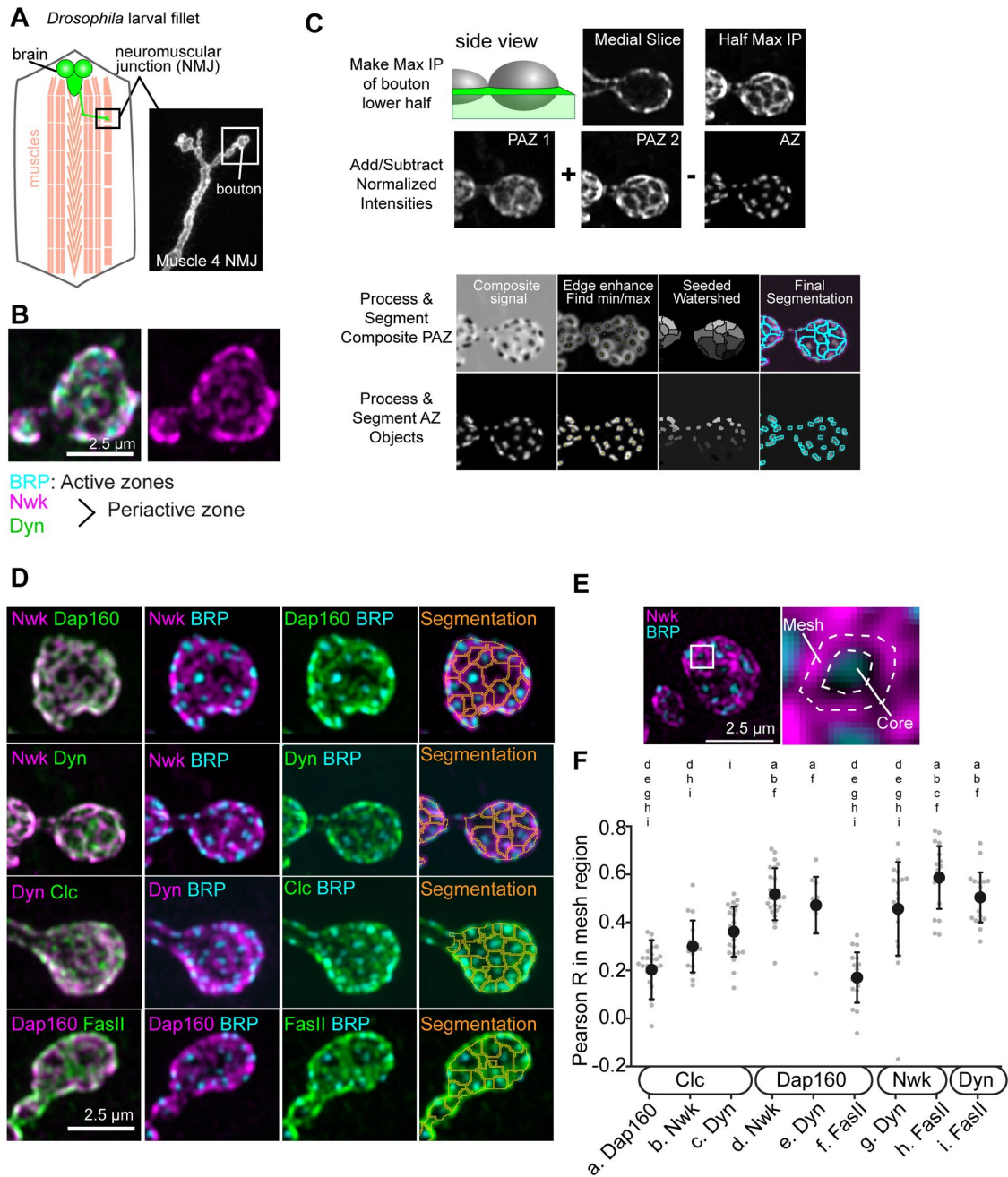
FIGURE 1: Endocytic proteins heterogeneously localize within the PAZ. (A) Schematic of the *Drosophila* NMJ prep. Left, cartoon illustration of the *Drosophila* larval fillet prep, with muscles highlighted in light red and the brain/motor neurons highlighted in green. Right, Example confocal image of a muscle 4 NMJ labeled with α-HRP. (B) Airyscan image of NMJ labeled with BRP (cyan), Nwk (magenta), and Dynamin (green). (C) Visualization of PAZ segmentation workflow. First, we generate maximum-intensity projections of boutons from the medial cross-section to the ventral surface of the neuron (i.e., the surface that is more deeply embedded in the muscle). To generate a composite segmentation, we normalize all channel intensities and add (PAZ) and subtract (active zone) channels to generate a single grayscale intensity map representing the NMJ. This image is then processed to enhance edge detection, and images are segmented by a watershed algorithm using local minima as seeds. For active zone object segmentation, local maxima are used as seeds followed by an additional distance transform watershed to separate touching objects. (D) The range of patterns of accumulation of endocytic proteins at the NMJ, as labeled. Note that Nwk and FasII form a more highly restricted mesh, Dynamin frequently intercalates into the core region, and Clc accumulates in a more punctate pattern. Right panels show example segmentations of the indicated channels into representative composite PAZ mesh. See *Materials and Methods* for more detail. (E) Schematic representation of a single PAZ mesh unit, divided into mesh and core regions. (F) Pearson *R* between the indicated pairwise comparisons within the mesh region indicates that colocalization of PAZ proteins is quite variable and ranges from low (~0.2) to moderately high (~0.6) but never approaches perfect or homogeneous colocalization. Letters above each group indicate which groups are significantly different from the given column at *p* < 0.05. Dots in F represent the average mesh value for a single image. Black dot and error bars indicate mean ± SD for all NMJs. For this and subsequent figures, see Supplemental Table S1 for a summary of number of animals, neurons, and PAZ units analyzed per experiment.
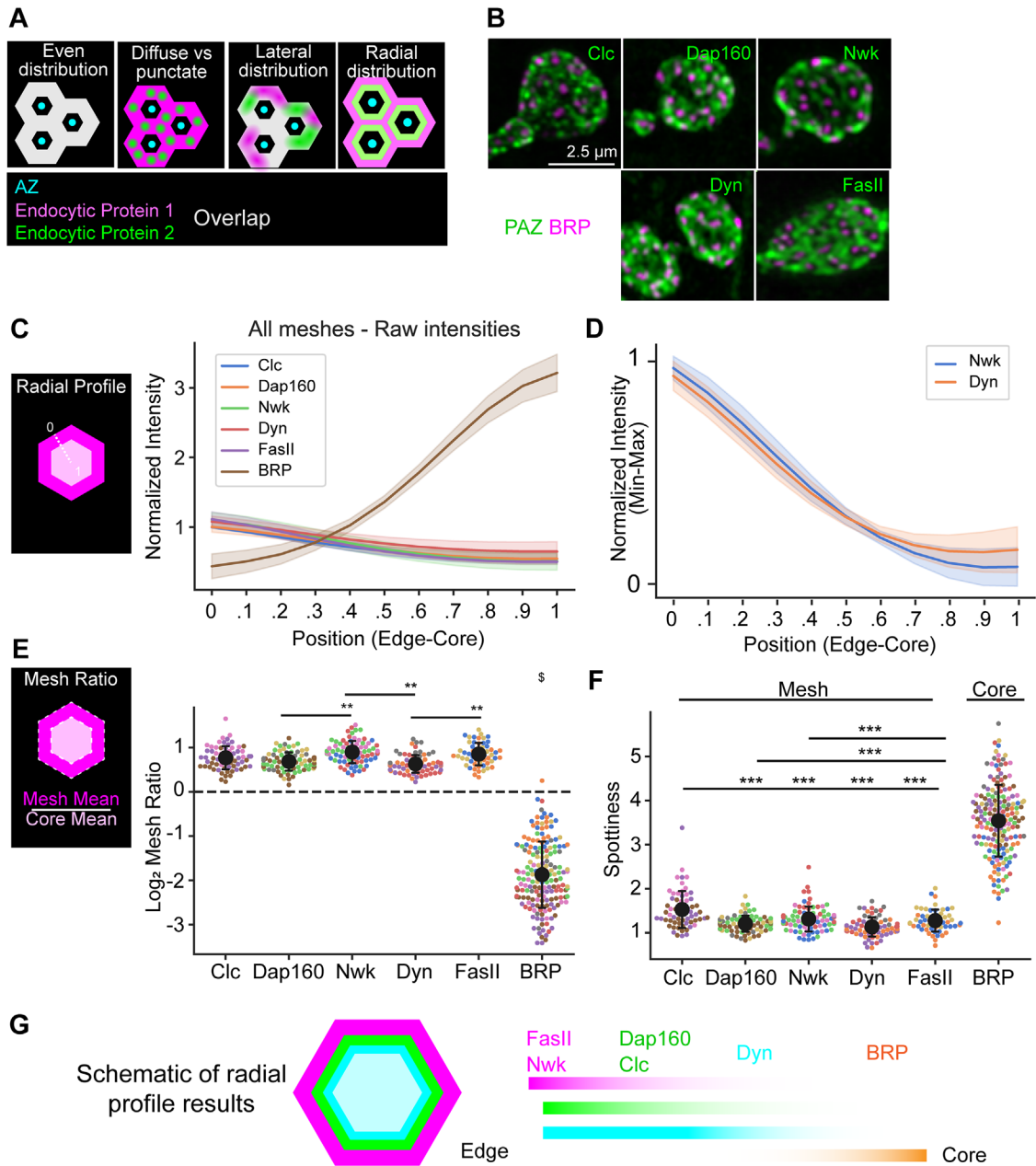
FIGURE 2: Endocytic proteins differentially distribute within the PAZ. (A) Cartoon illustrating potential ways that endocytic proteins might differentially accumulate—radially (from core to mesh), laterally (within the plane of the mesh region), or relatively more diffuse or punctate. (B) Example NMJ boutons labeled with BRP and single PAZ proteins to highlight differences in accumulation. (C, D) Radial profiles of BRP and PAZ proteins plotted against position from mesh edge (0) to core center (1), as depicted in the cartoon schematic. (C) Plots of mean normalized intensity by radial distance; BRP is inversely and more highly polarized compared with PAZ proteins. (D) Nwk and Dyn intensity (normalized min to max) plotted against radial position. Nwk is more highly polarized than Dyn, particularly at the core center. See Supplemental Figure S3 for all other pairwise profiles. (E) Quantification of the mesh ratio: the mean intensity in the mesh region divided by the mean intensity in the core, as depicted in the cartoon schematic. Nwk and FasII are significantly more enriched in the mesh than Dyn. (F) Quantification of 'spottiness," measured as the root mean squared of each image processed with a Laplacian of Gaussian filter. Higher values correspond to more punctate signal. (G) Cartoon summarizing radial distributions of PAZ and active zone proteins. Lines in C and D indicate the mean ± SD mesh profile from three to nine independent experiments per channel (see Supplemental Table S1 for details). $ in E indicates that BRP is significantly different from all other groups ($p < 0.001$). Dots in E and F represent the average mesh value for a single image; spot color indicates independent experimental replicates and does not correspond to colors in other figure legends. Black dot and error bars indicate mean ± SD for all NMJs.

(see *Materials and Methods* for details). As expected, we found that PAZ proteins were enriched in the mesh region and gradually tapered in the core. Conversely, the active zone protein BRP was strongly enriched in the PAZ core (Figure 2C) and tapered in the mesh region. We noted that the degree of radial polarization was much lower for PAZ proteins compared with BRP, suggesting a

nontrivial accumulation of PAZ proteins within the core region. Further, we noted small but significant differences in the degree of enrichment in the PAZ mesh between PAZ proteins—in particular, Dynamin had a significantly lower polarization than other PAZ proteins (Figure 2, C and D; Supplemental Figure S3A). To quantify these differences, we calculated the "mesh ratio," which is the ratio of the mean mesh intensity over the mean core intensity, and found that both Nwk and FasII were significantly more polarized than Dynamin (Figure 2E). This is consistent with our qualitative observations that Dynamin frequently accumulated within the core region adjacent to the active zone (Figure 2B) and may reflect a wider range of roles for Dynamin in vesicle recycling or a distinct mechanism of Dynamin recruitment relative to other endocytic proteins (see *Discussion*).

We next quantified how PAZ proteins accumulate within the mesh and core regions. We quantified the "spottiness" of protein distribution using a common spot detection filter (see *Materials and Methods* for details; Figure 2F). Owing to its purely punctate accumulation in the core region, BRP exhibited a much higher spottiness score than the PAZ proteins. Among PAZ proteins, we found that clathrin was significantly spottier than Dap160 and Dynamin (Figure 2F) within the mesh. We noted qualitatively that these clathrin puncta were far more numerous than the expected number of endocytic events at this synapse. We also analyzed the pixel intensity distribution more generally, using Haralick's entropy (Haralick *et al.*, 1973; Supplemental Figure S3B), which quantifies signal heterogeneity over a local spatial window. Consistent with its condensed/punctate accumulation, clathrin exhibited a significantly lower entropy score compared with the other PAZ proteins. Together, these data demonstrate that PAZ proteins exhibit both overlapping and distinct patterns of accumulation both radially and laterally at the PAZ (schematized in Figure 2G).

PAZ architecture does not perfectly align with active zone distribution

A conventional assumption regarding the PAZ is that it is defined spatially by the placement and patterning of active zones at the synaptic membrane. We sought to test this by comparing the micron-scale architectures defined by BRP-labeled active zones and by our composite PAZ. We selected BRP as an active zone marker because it has been extensively characterized at this synapse in structural (Kittel *et al.*, 2006; Fouquet *et al.*, 2009; Matkovic *et al.*, 2013; Böhme *et al.*, 2019) and physiological (Melom *et al.*, 2013; Akbergenova *et al.*, 2018; Böhme *et al.*, 2019) studies and at the resolution of our imaging forms a clear spot well suited for localization and intensity analyses. Functionally, BRP is a scaffold that is required for the maturation of active zones and the normal clustering of voltage-gated calcium channels (Kittel *et al.*, 2006; Fouquet *et al.*, 2009). First, we analyzed the spatial distributions of the local maxima of BRP with the local minima of our composite PAZ signal. We quantified the spatial patterning using Ripley's *g* function, which quantifies the fraction of points for which the nearest neighbor is within a given distance *d* (Figure 3, A and B). The spatial patternings of BRP and composite PAZ spots were indistinguishable. To determine the nature of this distribution, for each image analyzed we also created model point distributions generated by either purely random (Poisson), clustered (Poisson clustered), or regularly (Matern Type II) spaced processes (Figure 3A; see *Materials and Methods* for details and discussion of caveats). BRP and composite distributions most closely matched a regularly spaced distribution, with the minimum observed spacing between active zones of ~325 nm (Figure 3B). These data suggest that the relative placement of active zone/PAZ units is not random and that mechanisms exist to regulate their

spacing. Indeed these mechanisms may be linked, as PAZ mutants exhibit changes in active zone spacing (Dickman *et al.*, 2006).

We next asked how well each prospective method of synapse segmentation (active zone, PAZ, or composite) best represented the architecture of the entire synapse, that is, is the synapse best captured using only active zone signal, only the PAZ signal, or a composite of the two? To answer this question, we analyzed architecture agreement by Jaccard index (Figure 3C; Supplemental Figure S4, A and C) as well as a custom metric called centroid agreement, which measures the overlap between two sets of points by analyzing the average nearest-neighbor distance between each set of points compared with a theoretical null value for two sets of random points (Figure 3D; Supplemental Figure S4, B and D). As expected, the composite segmentation approach (which incorporates information from PAZ and active zone signals) did the best job of simultaneously representing both active zone and PAZ architectures: First, both Jaccard index and centroid agreement indicate that BRP and composite architectures agree only moderately. Second, we find that the composite mesh matches BRP and individual PAZ meshes similarly well, while the BRP mesh is significantly worse at representing each individual PAZ signal (compare blue to orange dots in Figure 3, C and D). Together, these data indicate that PAZ architecture reflects both active zone–dependent and -independent features and that the PAZ architecture is not purely defined by the active zone.

An obvious and intriguing example of the differences between these architectures is the existence of composite PAZ units containing zero or multiple active zones (Figure 3, E and F). We noted that while the majority of PAZ meshes contained exactly one active zone (57%), many contained zero (26%) or multiple (17%) active zones. Further, we noted that PAZ mesh size scaled with active zone number (Figure 3F). The assembly and composition of active zones change developmentally (Akbergenova *et al.*, 2018) and homeostatically (Weyhersmüller *et al.*, 2011; Böhme *et al.*, 2019; Hong *et al.*, 2020), including the formation of multiple linked active zones (Hong *et al.*, 2020). It will be interesting to determine the physiological properties of these multi–active zone PAZ units and to what extent these represent transient developmental or stable architectural features.

PAZ architecture correlates with active zone properties

We next asked whether PAZ domain architecture correlates with the properties of nearby active zones. Active zones at the *Drosophila* NMJ can vary >50-fold in their probability of vesicle release (Melom *et al.*, 2013; Akbergenova *et al.*, 2018). We noted that PAZ proteins also exhibited significant variability between PAZ mesh units, with a SD of ~25% of the mean intensity of each protein (Supplemental Figure S5A). Here we asked whether the abundance and distributions of PAZ proteins covaried with BRP abundance at the active zone (see schematic Figure 4A). This analysis takes advantage of the fact that the concentration of the scaffold protein BRP positively correlates with calcium channel numbers and active zone release probability (Melom *et al.*, 2013; Akbergenova *et al.*, 2018; Gratz *et al.*, 2019). To simplify the analysis, we focused on PAZ meshes containing exactly one active zone. We compared BRP abundance to 18 PAZ measurements including PAZ area, PAZ protein concentration and distribution, and protein colocalization. Many parameters exhibited a significant correlation to BRP abundance (Figure 4, B–E; Supplemental Figure S5B; Supplemental File 1). Most notably, we found that the concentration of PAZ proteins (measured as their mean intensity) in both core and mesh regions strongly correlated with BRP abundance, suggesting that the concentration of PAZ proteins increases as release probability increases. Notably, for the lone
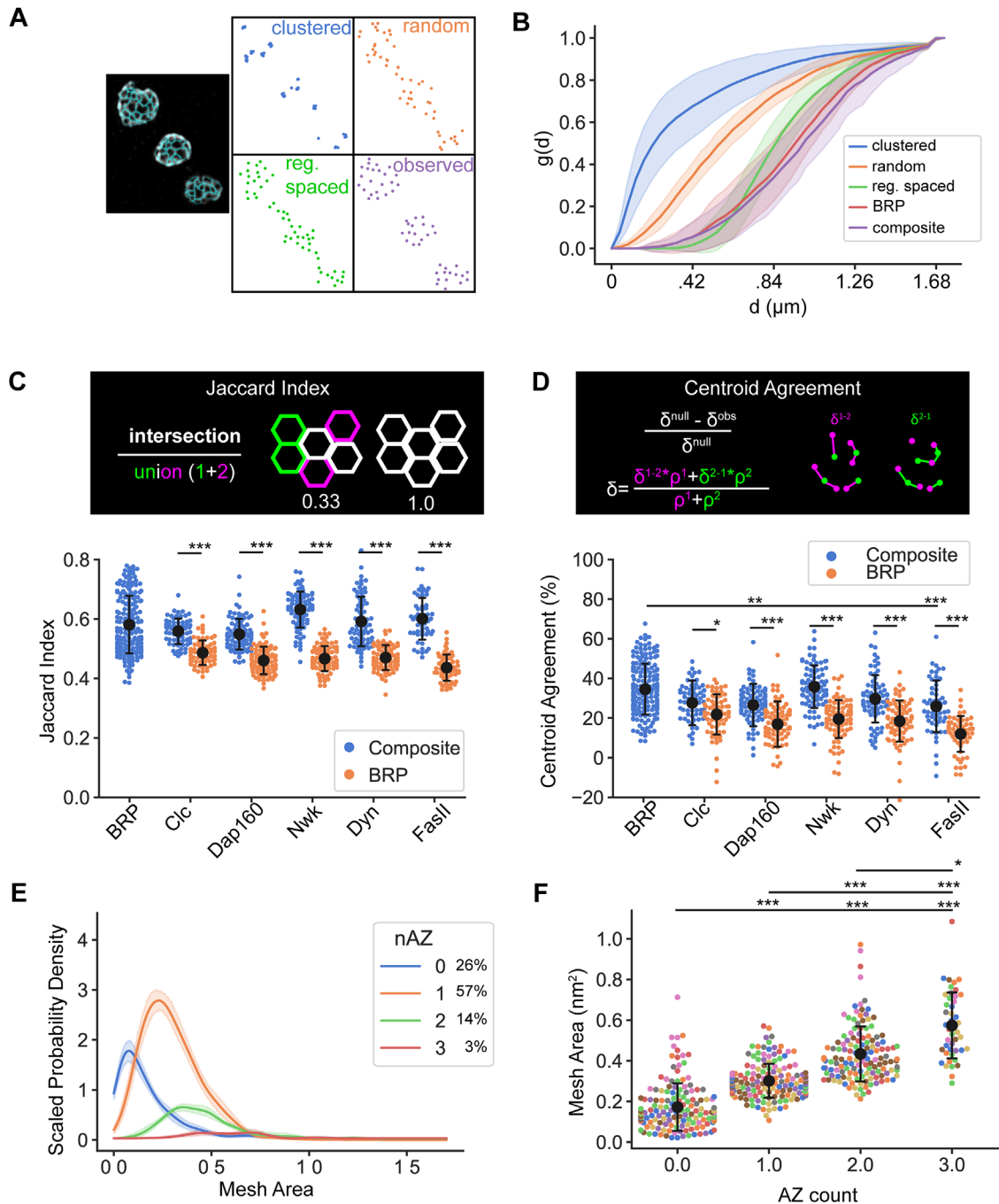
FIGURE 3: Active zone position and pattern only partially define PAZ architecture. (A, B) Example observed and model patterning of BRP and composite mesh centroids. (A) Left, Example NMJ with composite segmentation labeled in cyan. Right, Modeled clustered, regularly spaced, and random spatial point distributions for the example NMJ compared with the observed composite mesh centroid pattern. (B) Quantification of Ripley's *g* function shows that spatial patterning of BRP and composite segmentations are indistinguishable and best resemble a regularly spaced distribution. (C, D) Comparison of active zone and composite PAZ segmentations. Both Jaccard index (C) and centroid error (D) indicate that composite segmentations match active zone and individual PAZ meshes similarly well and significantly better than active zone–based segmentations. (E) Probability density estimates of mesh areas from composite-based segmentations, broken down by the number of active zones in the mesh. Active zone number correlates with mesh size. (F) Quantification of mesh area of composite meshes containing 0–3 active zones. The area of meshes significantly increases as active zone number increases. Dots in C and D represent the average value for a single image; black dot and error bars indicate mean ± SD for all images. Lines in B and E represent the mean ± SD per image (B) or experiment (E). Dots in F represent the average value for a single image; colors represent measurements made from independent experiments. Black dot and error bars indicate mean ± SD for all NMJs.
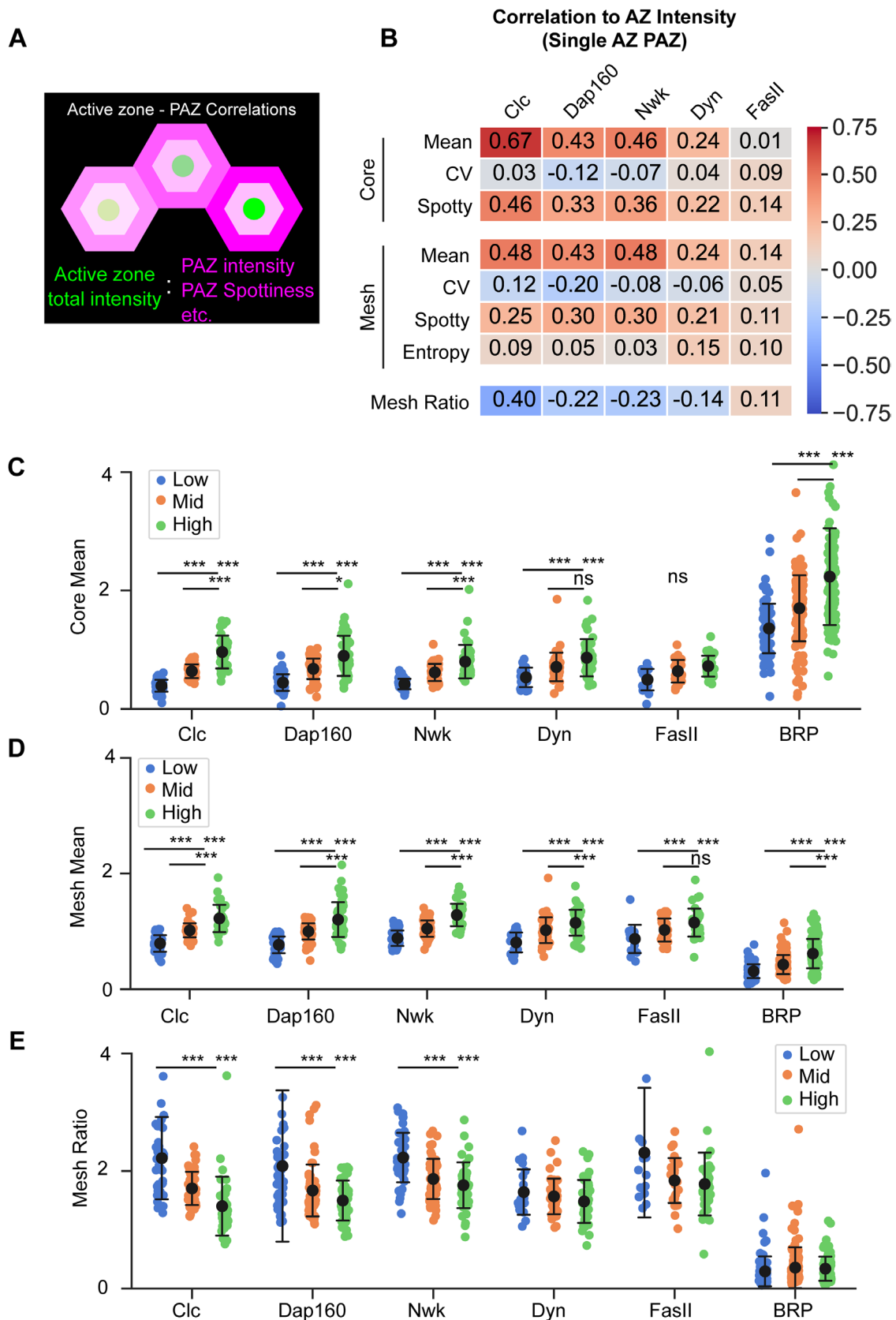
FIGURE 4: Synaptic endocytic protein architecture correlates with active zone structural properties. (A) Schematic of comparisons between active zone intensity and PAZ protein distributions. (B) Table summarizing the Pearson correlation between active zone integrated density and the indicated PAZ metrics. Notably, accumulations of all PAZ proteins except FasII in core and mesh regions generally correlate with active zone intensity. Mesh ratio exhibits a variable but generally negative correlation to active zone intensity. Additional metrics are shown in Supplemental

adhesion protein in our analysis (FasII), this correlation was either not observed (in the core region; Figure 4C) or strikingly lower (in the mesh region; Figure 4D), suggesting that this scaling may either be a specific property of endocytic PAZ proteins or perhaps reflects different levels of dynamics between the membrane-associated endocytic proteins and the transmembrane FasII. We also noted that the mesh ratio of Clc, Dap160, and Nwk exhibited a significant negative correlation with BRP abundance (Figure 4, B and E), while Dynamin and FasII do not, indicating that only a subset of endocytic proteins redistribute according to the composition or physiology of nearby active zones.

To validate our findings in fixed tissues, we measured the distribution and relationship of Nwk and BRP in living neurons by imaging Nwk and BRP labeled with HALO or GFP tags knocked in to the endogenous loci. We found that, as in fixed tissues, Nwk localized to a membrane proximal mesh surrounding active zones labeled with BRP (Figure 5, A and B). Radial profiles and mesh ratios were quantitatively similar to those observed in fixed samples (Figure 5, C and D), and relationships to BRP abundance were largely preserved (Figure 5, E and F). We did note small differences in the relationship between Nwk CoV and Entropy with BRP abundance, which might reflect some degree of temporal integration during fixation. In total, however, we conclude that our results are robust to live versus fixed imaging.

Finally, we tested the role of imaging modality on our analysis and conclusions. For these experiments we used STED microscopy to image Nwk or Dyn along with BRP (to compare active zone—PAZ distributions by STED; Figure 5, G–K). In each case, we found that the observations made by Airyscan confocal microscopy were well supported by STED imaging (Figure 5, H–K). STED microscopy better resolved differences in the distributions of the each of the proteins, such as the ring-like appearance of BRP labeled with the nc82 antibody, as previously described (Kittel et al., 2006; Fouquet et al., 2009). Notably, Dyn appeared as a dense collection of puncta (in contrast to the more continuous distribution by Airyscan), while Nwk appeared as a more continuous mesh, similar to that observed by Airyscan. In total, we conclude that our analysis pipeline can be readily applied to different superresolution imaging modalities (and resolutions).

DISCUSSION
Predeployment model for synaptic endocytic machinery
Endocytic proteins accumulate at vastly higher concentrations and across much broader domains at synaptic membranes compared with nonsynaptic membranes. Recent work suggests that a subset of endocytic proteins are predeployed to synaptic membranes (Del Signore et al., 2021; Imoto et al., 2022). Predeployment could provide an essential mechanism to allow for low latency vesicle recycling or release site clearance (Kawasaki et al., 2011), to build a large pool of molecules for high-capacity cargo binding and internalization, or for other emergent requirements such as limiting cargo diffusion (Azarnia Tehran and Maritzen, 2022). This predeployment suggests that different regulatory mechanisms may control the molecular dynamics and activation

of membrane remodeling at synapses compared with nonneuronal cells and could result from multiple mechanisms including specialized lipid domains (Khuong et al., 2010; Wahl et al., 2016; Li et al., 2020) or protein phase separation (Imoto et al., 2022; Kozak and Kaksonen, 2022). Yet to date most studies of synaptic endocytic protein dynamics have focused on global transitions between membrane compartments such as the synaptic vesicle pool and the plasma membrane (Bai et al., 2010; Denker et al., 2011; Winther et al., 2013, 2015; Li et al., 2020), general diffusion (Wilhelm et al., 2014; Reshetniak et al., 2020), or the axonal transport and synaptic retention of clathrin "packets" (Ganguly et al., 2021). There remain few data that show how the organization of endocytic proteins might drive synaptic vesicle recycling at different spatial and temporal scales. Our work provides the first quantitative analysis of the micron-scale architecture and nano-scale distribution of a subset of the endocytic machinery at a synapse and will be of great utility for understanding the distributions and regulation of dozens of additional components in future mechanistic studies. These analyses greatly extend prior qualitative descriptions of the micron-scale PAZ in both flies (González-Gaitán and Jäckle, 1997; Sone et al., 2000; Coyle et al., 2004; Marie et al., 2004; Rodal et al., 2008) and cultured mammalian neurons (Wilhelm et al., 2014; Gerth et al., 2017). Using our new method, we identify a novel and unexpected heterogeneity in the distribution of endocytic regulators *within* the PAZ and also between different active zones.

Spatial segregation of PAZ components
The dense accumulation of PAZ proteins renders it difficult to assign discrete molecular activities or synaptic functions to specific membrane domains or protein accumulations. Our approach addresses this issue by providing a granular, spatially resolved map of PAZ protein accumulation. We found that endocytic proteins exhibited distinct patterns of accumulation within the PAZ. Endocytic proteins localized with only partial overlap within the PAZ mesh (Figure 1F), differentially partitioned between active zone core and PAZ mesh domains (Figure 2E), and accumulated into relatively more diffuse or punctate patterns (Figure 2F; Supplemental Figure S3B). It will be interesting to determine the molecular composition and function of these distinct patterns: does punctate clathrin reflect predeployed but immature clathrin structures or assemblies (Henne et al., 2010; Brach et al., 2014; Ganguly et al., 2021; Wood and Smith, 2021)? Does stronger Dyn accumulation in the PAZ core reflect its roles in modes of endocytosis that occur proximal to release sites, including ultrafast endocytosis (Kosaka and Ikeda, 1983; Koenig and Ikeda, 1996; Teng and Wilkinson, 2000; Kidokoro, 2006; Kuromi et al., 2010; Watanabe et al., 2013a)? Are more peripheral PAZ proteins held in a "poised" or inactive state, or are they engaged in more diverse synaptic functions beyond synaptic vesicle endocytosis (O'Connor-Giles et al., 2008; Rodal et al., 2008, 2011; Gimber et al., 2015; Jäpel et al., 2020; Blanchette et al., 2022)? Alternatively, this heterogeneity could also reflect different temporal stages of a single biological process (such as stages of endocytosis). Finally, it will be important to investigate how spatial cues that regulate endocytic organization and function (such as

File 1. (C–E) Comparison of core mean intensity (C), mesh mean intensity (D), and mesh ratio (E) for PAZ and active zone proteins binned by active zone intensity quantile. (C, D) Consistent with Pearson values, in most cases PAZ proteins exhibit significantly higher core means in the high active zone intensity bin, with FasII a notable exception. (E) Clc, Dap160, and Nwk show a clear decrease in mesh enrichment as active zone integrated density increases. Values in B represent the average Pearson *R* per experiment, calculated from individual meshes of all images. Dots in C–E represent the average value per image; color indicates the active zone integrated density bin. Black dot and error bars indicate mean ± SD of all NMJs.
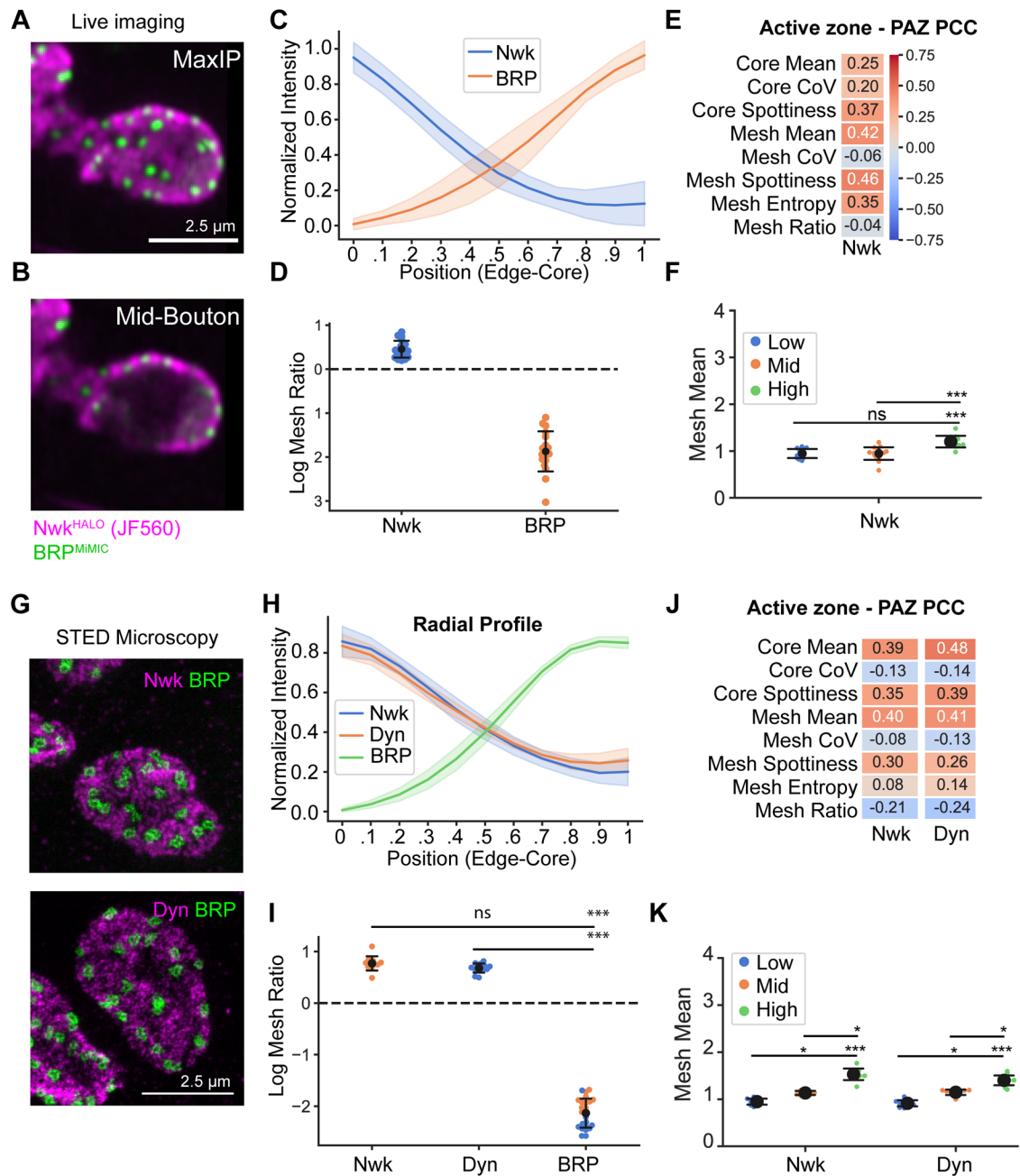
FIGURE 5: Live imaging and STED microscopy validate measurements of PAZ architecture. (A, B) Maximum-intensity projection (A) and mid–bouton plane of a muscle 4 bouton labeled with endogenously tagged Nwk[HALO] (JF549) and BRP[MiMIC]. (C, D) Quantifications of distribution of Nwk and BRP by radial profiling (C) and mesh ratio (D) show strong polarization of Nwk in the PAZ mesh and BRP in the PAZ core, consistent with observations in fixed tissues. (E, F) Comparison of Nwk and BRP intensity. Nwk accumulation and distribution correlate with BRP intensity, similar to results in fixed tissues. Correlations between BRP and Nwk CoV and Entropy differ slightly, suggesting that features of the Nwk distribution may be sensitive to fixation. (G–K) Imaging and analysis of PAZ architecture by STED microscopy. Nwk-BRP and Dyn-BRP comparisons were made in independent experiments. (G) Single plane 2D STED microscopy images of Nwk and BRP (top) or Dyn and BRP (bottom). (H, I) Radial distribution by radial profile (H) or mesh ratio (I) demonstrates that Nwk and Dyn are enriched in the PAZ mesh, while BRP is strongly enriched in the PAZ core, consistent with Airyscan microscopy. (J, K) Quantification of active zone intensity—PAZ relationships. Similar to Airyscan, Nwk and Dyn accumulation in both mesh and core correlates with active zone intensity.

lipid composition) are patterned in the PAZ (Khuong *et al.*, 2010; Wahl *et al.*, 2016; Li *et al.*, 2020). Our new quantitative framework represents a first essential step to describe the distributions of these proteins at synapses; future experimental studies that employ our strategy will help us understand their regulation and function at synapses. For example, our method will be useful for identifying where and how endocytic proteins dynamically localize to active endocytic membrane remodeling events, for example, by including markers of actin filament polymerization as a proxy for membrane invagination (Del Signore *et al.*, 2021).

Fly strain	Source	Identifier
yw; Mi{PT-GFSTF.1}nwk[MI05435-GFSTF.1] (Nwk^MiMIC)	Bloomington *Drosophila* Stock Center	RRID:BDSC_64445
y[1] w[67c23]; Mi{PT-GFSTF.0}brp[MI02987-GFSTF.0]/SM6a (Brp^MiMIC)	Bloomington *Drosophila* Stock Center	RRID:BDSC_59292
Elav[c155-GAL4]	Bloomington *Drosophila* Stock Center	RRID:BDSC_458
P{UAS-EGFP-Clc}5	Bloomington *Drosophila* Stock Center	RRID:BDSC_7109
dap160^Δ1	Bloomington *Drosophila* Stock Center	RRID:BDSC_24877
nwk^H-HALO	This study	
dap160^TSTEP	This study	

TABLE 2: *Drosophila* strains used in this study.

Correlation of active zone and PAZ architecture

We found that the architecture and distribution of the endocytic machinery correlates with the functional properties of nearby sites of exocytosis (Figure 4, B–E). It remains to be determined whether the coordination between PAZ and active zones in our experiments reflects acute or developmental adaptation of the endocytic machinery to vesicle release, or conversely, a role for the endocytic machinery in the assembly of active zones. Either may be likely as there are multiple examples of bidirectional cross-talk between active zones and PAZ: First, calcium influx via active zone–associated channels is thought to regulate endocytosis (Jorgensen *et al.*, 1995; Littleton *et al.*, 2001; Poskanzer *et al.*, 2003, 2006; Nicholson-Tomishima and Ryan, 2004; Wu *et al.*, 2009; Yao *et al.*, 2011). Second, membrane lipids may coordinately regulate synaptic vesicle exocytosis (Honigmann *et al.*, 2013; Khuong *et al.*, 2013; Walter *et al.*, 2017; Maritzen and Haucke, 2018) and endocytosis (Cremona *et al.*, 1999; Verstreken *et al.*, 2003; Di Paolo *et al.*, 2004; Posor *et al.*, 2013). Third, endocytic mutants increase the density of active zones at synaptic membranes (Dickman *et al.*, 2006; Goel *et al.*, 2019), supporting an instructive role for the PAZ machinery in active zone development. Finally, endocytic proteins play moonlighting roles in rapid clearance of *cis*-SNARE complexes from release sites (Kawasaki *et al.*, 2000; Hosoi *et al.*, 2009; Neher, 2010; Hua *et al.*, 2013; Sakaba *et al.*, 2013; Wu *et al.*, 2014; Jäpel *et al.*, 2020) to allow for high-frequency exocytosis. Our analytical framework provides new opportunities to directly quantify the spatial and temporal relationship between exocytosis and endocytic molecular dynamics both during development and in mutants that perturb synaptic activity and endocytic function.

MATERIALS AND METHODS

Request a protocol through *Bio-protocol*.

***Drosophila* imaging.** Flies were cultured using standard media and techniques. All flies were raised at 25°C. See Table 2 for fly strains used in this work.

Immunohistochemistry. For analysis of NMJ morphology and protein localization, flies were cultured at low density at 25°C. Wandering third instar larvae were dissected in calcium-free HL3.1 saline (Feng *et al.*, 2004) and fixed for 20 min in HL3.1 containing 4% formaldehyde. Fixed larvae were blocked in 3% bovine serum albumin in 0.1% Triton X-100 in phosphate-buffered saline for 30–60 min and incubated with primary antibody in block solution either overnight at 4°C or 2 h at room temperature, followed by washing and incubation with dye-conjugated secondary antibodies (Jackson Immunoresearch). Larvae were mounted in Prolong Diamond mounting medium. Primary antibodies used were rabbit anti-Nwk 970 (RRID:AB_2567353 [Coyle *et al.*, 2004]), rabbit anti-Dap160 (RRID:AB_2569367 [Roos and Kelly, 1998]), rabbit anti-Dyn (RRID:AB_2314348 [Estes *et al.*,

1996]), mouse anti-Dyn (RRID:AB_397640; BD Biosciences Clone 41), mouse anti-BRP (RRID:AB_2314866; Developmental Studies Hybridoma Bank [DSHB] clone nc82), mouse anti-FasII (RRID:AB_528235 [DSHB clone 1D4]), and goat anti–horseradish peroxidase (HRP) directly conjugated to rhodamine Red-X (RRID AB_2338964). For Airyscan imaging, larvae were minimally stretched and mounted in an excess volume of mounting medium to preserve three-dimensional (3D) morphology of boutons. For STED imaging, larvae were stretched and mounted in a minimum volume of medium (approximately 30 µL) to render preparations flat to aid 2D imaging. Live HALO labeling of Nwk^HALO was performed as follows: we dissected heterozygous Nwk^HALO/+ larvae in HL3.1 medium, incubated fillets in 250 nM HALO ligand-JF646 (Promega) for 5 min, washed them in HL3.1 for 5 min, and then mounted and imaged the fillets immediately. All live preps were mounted in a sandwich formed by a coverslip mounted on a slide, spaced by two pieces of double-sided tape (3M), and imaged within 15 min of mounting.

FM1-43 uptake. FM uptake was adapted from Verstreken *et al.* (2008). Larvae were dissected in HL3 medium containing 5 mM KCl and 0 mM CaCl$_2$ (HL3). To label the synaptic vesicle pool, fillets were then incubated in HL3 containing 90 mM KCl, 2 mM CaCl$_2$, and 4 µM FM1-43 for 5 min at room temperature. Fillets were rinsed three times in HL3 and then incubated in HL3 containing 200 nM JF646 HALO ligand for 2 min at room temperature to label Nwk^HALO. Fillets were rinsed three times and then washed twice for 5 min in HL3 before live imaging.

Image acquisition. Confocal and Airyscan images of NMJs were acquired with a Zeiss 880FAS microscope with a 63× (NA1.4) oil immersion objective in LSM or SR mode, respectively, using Zen Blue software. All raw image stacks were processed in Zen Blue to construct Airyscan images using 3D Airyscan processing with automatic settings. We quantified optical resolution using tetraspeck beads (Invitrogen) at 560 nm as $158 \times 179 \times 401$ nm in *XYZ*, respectively. We found this resolution to be sufficient to subdivide the PAZ, localize active zone and PAZ components, and generate radial profiles of PAZ units and provide results consistent with STED microscopy (see Figure 5). To image anti–HRP-labeled extracellular vesicles, confocal stacks of larval fillets were acquired on a Marianas spinning-disk confocal system (3I, Denver, CO), consisting of a Zeiss Observer Z1 microscope equipped with a Yokagawa CSU-X1 spinning-disk confocal head, a QuantEM 512SC EMCCD camera, PLAN APOCHROMAT 63× oil immersion objectives (NA 1.4), and Slidebook software.

2D-STED images were acquired with an Abberior FACILITY line STED microscope with 60× (NA1.3) silicone immersion objective, pulsed excitation lasers (561 and 640 nm), and a pulsed depletion laser (775 nm) used to deplete all signals. BRP was labeled with STAR RED (Abberior), and both Nwk and Dyn were labeled with

STAR ORANGE (Abberior). Pixel size was set to 30 nm, and single 2D slices were acquired of terminal branches of NMJs that lay in a single focal plane. All images within one data set were acquired with the same microscope settings (see Supplemental Table S1 for numbers of technical and biological replicates).

Generation of Dap160^TSTEP. The endogenous *dap160* locus was tagged with a tissue-specific convertible TagRFPt to EGFP tag (T-STEP [Koles *et al.*, 2015]). Briefly, the following genomic sequence was used to target Cas9 cleavage: ATGTGAGATTCACTTCTTG-GTGG (at location 2L:21139297–21139319). The T-STEP cassette was flanked with 5′ homology (2L:21138474-21139307) and 3′ homology (2L:21139308-21140194) arms, and gene targeting was carried out as described (Koles *et al.*, 2015, based on Chen *et al.*, 2015). Dap160-TSTEP flies were crossed to C380-Gal4;;UAS-Rippase::PEST @attP2 flies to isolate motor neuron ripouts of the TagRFPt cassette, leaving a C-terminal EGFP knockin.

Generation of Nwk-Halo. A HALO7 tag was knocked into the endogenous locus by CRISPR-CAS9 mediated gene editing (performed by Wellgenetics, using modified methods of Kondo and Ueda (2013). In brief, guide RNA sequence AGCCACGGACAGTTATAGAG[CGG] was cloned into U6 promoter plasmid(s). This targets the stop codon in exon 22, thus labeling isoforms H, I, J, and L. Cassette Halo7-3xP3-RFP, which contains Halo7 and a floxed 3xP3-RFP, and two homology arms were cloned into pUC57-Kan as donor template for repair. nwk/CG43479-targeting gRNAs and hs-Cas9 were supplied in DNA plasmids, together with donor plasmid for microinjection into embryos of control strain w[1118]. F1 flies carrying selection marker of 3xP3-RFP were further validated by genomic PCR and sequencing. CRISPR generates a break in nwk/CG43479 and is replaced by cassette Halo7-3xP3-RFP. Finally, the floxed 3xP3-RFP cassette was excised to generate the knockin strain used in experimental crosses.

Validation of knockin reagents. To test whether knockin reagents (Nwk^MiMIC, Nwk^HALO, and Dap160^TSTEP) recapitulated the localization of labeling of endogenous protein by antibody labeling, we performed colabeling of knockin lines with the respective antibody (Supplemental Figure S2, A and B). We tested Nwk knockins as homozygotes and tested the Dap160^TSTEP as a heterozygote, both over a wild-type allele and over the *dap160^1* mutant allele. The former genotype tests whether the knockin exhibits a different pattern compared with an untagged allele, while the latter condition assesses the specificity of the antibody. In each case we observed a very high (>0.8) Pearson's *R*, indicating good, though not perfect, agreement between the labeling strategies. To test whether knockins were functional, we measured the accumulation of postsynaptic anti–HRP-labeled extracellular vesicles, which we have previously shown are highly sensitive to loss of function of these proteins (Supplemental Figure S2, C and D [Blanchette *et al.*, 2022]). We found that the Nwk^MiMIC allele did represent a significant loss of function, despite its normal localization, while the other knockins were not detectably different from controls. All together and considering the high degree of agreement between labeling strategies in our PAZ analyses (see *Results*), we conclude that each of these knockins faithfully recapitulates endogenous protein localization patterns, though we conclude that the Nwk^MiMIC allele would be compromised with respect to any functional study.

Quantification of extracellular vesicle phenotypes. Muscle 4 NMJs (abdominal segments 3 and 4) were imaged by spinning-disk confocal microscopy. Images were manually cleaned to remove

axon or nonsynaptic debris. Using a custom FIJI script (available at https://github.com/rodallab/paz-analysis), NMJs were segmented by intensity to create a 3D mask of the presynaptic terminal. A second mask was generated by intensity to include presynaptic HRP as well as postsynaptic HRP-labeled extracellular vesicles. Extracellular vesicle signal was considered to be any postsynaptic signal within 3.5 microns of the presynaptic mask. The total integrated density of this postsynaptic signal was then normalized to the volume of the presynaptic terminal. All data shown were further normalized to the average of the control *white* genotype.

PAZ processing and segmentation
All image processing and data extraction were performed using custom FIJI and Python scripts (available at https://github.com/rodallab/paz-analysis).

Image preprocessing. Before PAZ segmentation and analysis, 2D maximum-intensity projections of the bottom half of NMJ boutons were made semimanually using a custom FIJI script as follows: regions of interest were drawn manually around boutons lying in the same approximate *Z* plane, and the medial Z-slice was set. Maximum-intensity projections of the lower portions of the stack were generated and saved, and the medial slice was also saved. As needed, images were manually "cleaned" to remove axon or other spurious signal not belonging to a Type 1b motor neuron.

NMJ segmentation. Segmentations of the entire bouton region(s) within each image were performed as follows: 1) Whole stacks were background subtracted (rolling ball radius = 50 pixels). 2) Channel intensities were normalized by the whole-image average value per channel. 3) All channels were summed to create a composite NMJ image. 4) The composite image was blurred using a Gaussian filter (sigma = 1). 5) The image was autothresholded using the Li algorithm (Li and Tam, 1998). 6) The mask was eroded three times to better align the mask boundary with the NMJ membrane.

Generation and evaluation of composite and individual PAZ segmentations. We considered three basic approaches to segmenting the PAZ. First, we considered segmenting individual PAZ channels into meshes. The advantage of this approach is that it allows for a comparison of architectures for individual proteins. However, this approach had limitations as well because our goal was to conceptualize the PAZ as a unified membrane domain in which many of these proteins physically interact at some point in time and space. Further, individual PAZ representations matched each other poorly (see below) and made it difficult to directly compare different PAZ protein concentrations, colocalizations, and relationships to active zone properties. To solve these issues, we next considered segmenting the PAZ using the active zone as a fiduciary marker for the PAZ. This creates a unified PAZ representation, which simplifies PAZ–PAZ and active zone–PAZ comparisons, but necessarily misses some features of the PAZ, such as PAZ units with multiple active zones. Finally, we developed a composite PAZ segmentation strategy that accounts for both the PAZ and active zone signals in each experiment.

Segmentation of each NMJ into a PAZ mesh representation was performed as follows and is shown in Figure 1C: 1) The image stack was background subtracted (rolling ball radius = 50 pixels). 2) Individual channels were normalized by the minimum and maximum intensities per channel within the masked NMJ regions. 3) The image was blurred using a Gaussian filter (sigma = 1). 4) (Unique to the composite PAZ approach) PAZ channels were summed and the active zone channel subtracted to create a composite intensity image

(resulting in an image different from the composite for NMJ segmentation because here we subtract the active zone signal). The composite image was then processed with an "internal gradients" filter using an octagonal element of radius 5 (Legland *et al.*, 2016). 5) Local minima were detected using an empirically optimized threshold value (see below). 6) Mesh regions were identified using a marker-controlled watershed algorithm (Legland *et al.*, 2016). Individual channel segmentations were generated as above but using only single channels and with an internal gradient radius of 4. For each experiment, the composite mesh was defined by the composite of two PAZ proteins and BRP. All pairwise PAZ groups were represented across all experiments, and we did not observe experiment-to-experiment variability in the segmentation or metrics (Figures 2, E and F, and 3F; Supplemental Figures S4, A–D, and S5B), indicating that this strategy was robust to the specific PAZ channels used for segmentation. For analysis, the mesh region was considered a four-pixel-wide area around the PAZ unit boundary (six-pixel-wide for STED), and the core was considered to be the remaining area within the PAZ unit.

When evaluating the different segmentation strategies, we observed that individual PAZ meshes correlated poorly with one another (Supplemental Figure S6, A and B), reflecting the complex and heterogeneous distribution of endocytic proteins. The strictly active zone–based PAZ also correlated poorly with individual PAZ protein segmentation and was oversegmented due to the presence of a significant number of meshes with multiple active zones. The composite mesh segmentation most consistently represented active zone and PAZ architecture (Figure 3). Thus, we chose to use a composite mesh segmentation for all analyses where we compare different PAZ proteins (Figures 2–5). See shared Jupyter notebook for all details.

Segmentation of active zone mesh and objects. Segmentation of a mesh representation based on active zones (as discussed above) was performed as for single PAZ channel segmentations, except that local intensity maxima were detected rather than local intensity minima. Local maxima were used both to generate the active zone–based mesh and to localize and count active zones within PAZ meshes. For segmentation into active zone objects, these local maxima were used as seeds to generate objects by the seeded region growing ImageJ plugin (ImageJ-Plugins). Merged active zones were split by a distance transform watershed (Legland *et al.*, 2016).

Optimization of threshold value for min/max detection. The primary flexible parameter used to tune the segmentation of PAZ mesh is the tolerance/threshold value for the detection of local minima. A higher tolerance leads to a coarser segmentation (larger and fewer meshes), while a lower tolerance leads to a finer segmentation (small and more numerous meshes). To ensure consistent segmentation from image to image and experiment to experiment, we devised an optimization protocol to determine this threshold in an objective, unbiased manner. For each independent experiment, composite meshes were generated for each image using a wide range of tolerance values. The mesh generated by each (excluding meshes at the extreme edges of the NMJ [see below]) was used to measure the mesh ratio and average mesh size. Each image was scored as the geometric mean of mesh ratio, mesh area, and a spatial penalty representing the fraction of the NMJ that was effectively represented by the mesh. The spatial penalty was devised to prevent systematic oversegmentation of the NMJ. For each image, every tolerance value was ranked by score and the tolerance value with the best average rank was selected as the threshold for the entire experiment and applied to all images in that experiment. An identical process was used to optimize segmentation of individual channels.

Filtering of edge units. While generating and analyzing PAZ meshes, we observed a noticeable edge artifact in most images due to generating a flat 2D representation of a 3D ellipsoid. We observed this artifact as a higher-intensity (due to the summation of fluorescence along the vertical NMJ membrane by the point spread function) and an apparent higher number of active zones (due to the projection of active zones along the vertical surfaces of the NMJ). To exclude these edge effects from our analyses, we excluded all mesh units that occupied the edges of the NMJ (which we defined as having an average distance map value of 300 nm from the NMJ edge).

Quantification of PAZ architecture
Code used to perform all analyses in this article is freely available (https://github.com/rodallab/paz-analysis).

Jaccard index. The Jaccard index was calculated as the area of intersection of two meshes (with a mesh width of 2 pixels) divided by the area union of two meshes.

Centroid agreement. Centroid agreement quantifies the degree of overlap between two sets of points A and B (having number densities ρ^A and ρ^B, respectively). First, we calculated the average distance $\delta^{A,B}$ from each point in A to its nearest neighbor in B and the average distance $\delta^{B,A}$ from each point in B to its nearest neighbor in A. δ^{total} was calculated as the density-weighted average of $\delta^{A,B}$ and $\delta^{B,A}$, that is, $\delta^{total} = (\rho^A \delta^{A,B} + \rho^B \delta^{B,A})/(\rho^A + \rho^B)$. As a negative control, we compared δ^{total} to the situation of independent sets of regularly spaced points. We calculated this quantity explicitly in the case of a null model in which each of A and B is made up of points on a hexagonal lattice, with a random overall shift between the two lattices. We label the value obtained by this null model as δ^{null}: it may be shown by direct calculation that a very good approximation is obtained by setting $\delta^{null} = 0.4 (\rho^A/\sqrt{(\rho^B)} + \rho^B/\sqrt{(\rho^A)})/(\rho^A + \rho^B)$. We then define the centroid agreement as the relative difference from this null model: $(\delta^{total} - \delta^{null})/\delta^{null}$ (see Figure 3D).

Radial profiling. Radial profiles were calculated per mesh unit as the average of all intensity profiles drawn from each mesh pixel to the local intensity minimum of the mesh unit. To average across mesh units, distance values were normalized from 0 (mesh edge) to 1 (core minimum). To prevent artifacts due to small mesh units, we excluded from this analysis any mesh with an area less than 250 nm^2.

Haralick's entropy. Entropy was calculated using the ImageJ plugin "Texture Analyzer" (developed by Julio E. Cabrera). To calculate entropy, circular meshes were first transformed into rectangles using the "Straighten" function in ImageJ.

Spottiness. We processed images with a commonly used spot detection filter (Laplacian of Gaussian) and calculated the magnitude of response to this filter as the root-mean-squared value of the filtered image (because the filter ranges from positive to negative across spot boundaries). Higher scores indicate a more punctate or spotty distribution of signal.

Centroid distributions. Centroid distributions were measured in Python using PySal and pointpats libraries. First an alpha shape for each image was calculated using the pooled local minima

(PAZ channels or composite) and maxima (for active zone) per image. Ripley's g was calculated for composite or active zone point distributions. To determine the nature of the observed distribution, we generated model random, regularly spaced, or clustered distributions, each with a density matching the observed density (ρ^{obs}). Random and clustered were generated using pointpats from poisson and poisson cluster process, respectively. Clustered distributions were generated in two rounds, an initial "parent" round with an initial density of $(\rho^{obs})^{1/2}$. Next, a cluster radius r was defined as the area of the alpha shape divided by 512. Finally, each parent generated a sufficient number of "children" within a random radius on the interval 0–r to match ρ^{obs}. Regularly spaced distributions were generated by a Matern Type II process using code adapted from H. Paul Keeler (https://hpaulkeeler.com/simulating-matern-hard-core-point-processes/). One caveat of this approach is that modeled distributions were generated using the alpha mask as the boundary, which can be slightly broader than the actual NMJ area.

Colocalization. Pearson's correlations coefficients (PCC) were measured on 2D maximum-intensity projection images. As observed in medial slices (Figure 1A), the majority of PAZ signal is localized to the plasma membrane within our (X, Y) imaging resolution. As our imaging modalities have even less resolution in the Z, the maximum-intensity projection of our image half-stacks does not sacrifice any spatial information while allowing us to specifically address the lateral organization of PAZ proteins and their colocalization in the plane of the membrane. In some cases (Supplemental Figure S2, A and B), image channels were registered to correct for slight misalignment, using custom Python and FIJI scripts.

Statistical analysis

Graphs were prepared and statistical analyses performed with Python (using Matplotlib, Seaborn, Scipy-Stats, Scikit-Posthocs libraries). For normally distributed data, comparisons were made using either a T test or analysis of variance with posthoc Bonferroni's multiple comparisons test. For nonnormally distributed data, comparisons were made using a Mann–Whitney U test or a Kruskal–Wallis test with posthoc Dunn's test. All quantitative analyses presented were performed on data sets composed of two PAZ channels and BRP, imaged by Airyscan in SR mode. As we observed low between-experiment variability (as shown on plots), statistical comparisons are made using pooled data from multiple experiments. For the specific proteins labeled in each individual experiment and the number of animals, neurons, and PAZ units analyzed in each independent experiment please see Supplemental Table S1. No specific power analyses were performed; sample sizes were chosen based on established protocols and statistical analyses for significance, as detailed for all experiments here. See "Supplemental File 2-Statistical Analyses.zip" for each statistical test performed for each experiment presented in this study. Statistical significance denoted in all graphs: * $p < 0.05$, ** $p < 0.01$, *** $p < 0.001$.

REFERENCES

Akbergenova Y, Cunningham KL, Zhang YV, Weiss S, Littleton JT (2018). Characterization of developmental and molecular factors underlying release heterogeneity at Drosophila synapses. eLife 7, e38268.

Almeida-Souza L, Frank RAW, García-Nafría J, Colussi A, Gunawardana N, Johnson CM, Yu M, Howard G, Andrews B, Vallis Y, McMahon HT (2018). A flat BAR protein promotes actin polymerization at the base of clathrin-coated pits. Cell 174, 325–337.e14.

Azarnia Tehran D, Maritzen T (2022). Endocytic proteins: an expanding repertoire of presynaptic functions. Curr Opin Neurobiol 73, 102519.

Bai J, Hu Z, Dittman JS, Pym ECG, Kaplan JM (2010). Endophilin functions as a membrane-bending molecule and is delivered to endocytic zones by exocytosis. Cell 143, 430–441.

Bailey CH, Chen M, Keller F, Kandel ER (1992). Serotonin-mediated endocytosis of apCAM: an early step of learning-related synaptic growth in aplysia. Science 356, 645–649.

Becalska AN, Kelley CF, Berciu C, Stanishneva-Konovalova TB, Fu X, Wang S, Sokolova OS, Nicastro D, Rodal AA (2013). Formation of membrane ridges and scallops by the F-BAR protein Nervous Wreck. Mol Biol Cell 24, 2406–2418.

Beck ES, Gasque G, Imlach WL, Jiao W, Jiwon Choi B, Wu P-S, Kraushar ML, McCabe BD (2012). Regulation of Fasciclin II and synaptic terminal development by the splicing factor beag. J Neurosci 32, 7058–7073.

Blanchette CR, Scalera AL, Harris KP, Zhao Z, Dresselhaus EC, Koles K, Yeh A, Apiki JK, Stewart BA, Rodal AA (2022). Local regulation of extracellular vesicle traffic by the synaptic endocytic machinery. J Cell Biol 221, e202112094.

Bloom O, Evergren E, Tomilin N, Kjaerulff O, Löw P, Brodin L, Pieribone VA, Greengard P, Shupliakov O (2003). Colocalization of synapsin and actin during synaptic vesicle recycling. J Cell Biol 161, 737–747.

Böhme MA, McCarthy AW, Grasskamp AT, Beuschel CB, Goel P, Jusyte M, Laber D, Huang S, Rey U, Petzoldt AG, et al. (2019). Rapid active zone remodeling consolidates presynaptic potentiation. Nat Commun 10, 1085.

Brach T, Godlee C, Moeller-Hansen I, Boeke D, Kaksonen M (2014). The initiation of clathrin-mediated endocytosis is mechanically highly flexible. Curr Biol 24, 548–554.

Cano R, Tabares L (2016). The active and periactive zone organization and the functional properties of small and large synapses. Front Synaptic Neurosci 8, 12.

Chen H-M, Huang Y, Pfeiffer BD, Yao X, Lee T (2015). An enhanced gene targeting toolkit for Drosophila: Golic+. Genetics 199, 683–694.

Coyle IP, Koh Y-H, Lee W-CM, Slind J, Fergestad T, Littleton JT, Ganetzky B (2004). Nervous wreck, an SH3 adaptor protein that interacts with Wsp, regulates synaptic growth in Drosophila. Neuron 41, 521–534.

Cremona O, Di Paolo G, Wenk MR, Lüthi A, Kim WT, Takei K, Daniell L, Nemoto Y, Shears SB, Flavell RA, et al. (1999). Essential role of phosphoinositide metabolism in synaptic vesicle recycling. Cell 99, 179–188.

Dagar S, Teng Z, Gottmann K (2021). Transsynaptic N-cadherin adhesion complexes control presynaptic vesicle and bulk endocytosis at physiological temperature. Front Cell Neurosci 15, 399.

Davis GW, Goodman CS (1998). Synapse-specific control of synaptic efficacy at the terminals of a single neuron. Nature 392, 82–86.

Del Signore SJ, Kelley CF, Messelaar EM, Lemos T, Marchan MF, Ermanoska B, Mund M, Fai TG, Kaksonen M, Rodal AA (2021). An autoinhibitory clamp of actin assembly constrains and directs synaptic endocytosis. eLife 10, e69597.

Denker A, Bethani I, Kröhnert K, Körber C, Horstmann H, Wilhelm BG, Barysch SV, Kuner T, Neher E, Rizzoli SO (2011). A small pool of vesicles maintains synaptic activity in vivo. Proc Natl Acad Sci USA 108, 17177–17182.

Denker A, Kröhnert K, Rizzoli SO (2009). Revisiting synaptic vesicle pool localization in the Drosophila neuromuscular junction. J Physiol 587, 2919–2926.

Dickman DK, Lu Z, Meinertzhagen IA, Schwarz TL (2006). Altered synaptic development and active zone spacing in endocytosis mutants. Curr Biol 16, 591–598.

Di Paolo G, Moskowitz HS, Gipson K, Wenk MR, Voronov S, Obayashi M, Flavell R, Fitzsimonds RM, Ryan TA, De Camilli P (2004). Impaired PtdIns(4,5)P2 synthesis in nerve terminals produces defects in synaptic vesicle trafficking. Nature 431, 415–422.

Estes PS, Roos J, Bliek Av, Kelly RB, Krishnan KS, Ramaswami M (1996). Traffic of dynamin within individual Drosophila synaptic boutons relative to compartment-specific markers. J Neurosci 16, 5443–5456.

Evergren E, Marcucci M, Tomilin N, Löw P, Slepnev V, Andersson F, Gad H, Brodin L, De Camilli P, Shupliakov O (2004). Amphiphysin is a component of clathrin coats formed during synaptic vesicle recycling at the lamprey giant synapse. Traffic 5, 514–528.

Feng Y, Ueda A, Wu C-F (2004). A modified minimal hemolymph-like solution, HL3.1, for physiological recordings at the neuromuscular junctions of normal and mutant Drosophila larvae. J Neurogenet 18, 377–402.

Fouquet W, Owald D, Wichmann C, Mertel S, Depner H, Dyba M, Hallermann S, Kittel RJ, Eimer S, Sigrist SJ (2009). Maturation of active zone assembly by Drosophila Bruchpilot. J Cell Biol 186, 129–145.

Fu Y, Huang ZJ (2010). Differential dynamics and activity-dependent regulation of α- and β-neurexins at developing GABAergic synapses. Proc Natl Acad Sci USA 107, 22699–22704.

Gan Q, Watanabe S (2018). Synaptic vesicle endocytosis in different model systems. Front Cell Neurosci 12, 171.

Ganguly A, Sharma R, Boyer NP, Wernert F, Phan S, Boassa D, Parra L, Das U, Caillol G, Han X, et al. (2021). Clathrin packets move in slow axonal transport and deliver functional payloads to synapses. Neuron 109, 2884–2901.e7.

Gerth F, Jäpel M, Pechstein A, Kochlamazashvili G, Lehmann M, Puchkov D, Onofri F, Benfenati F, Nikonenko AG, Fredrich K, et al. (2017). Intersectin associates with synapsin and regulates its nanoscale localization and function. Proc Natl Acad Sci USA 114, 12057–12062.

Ghelani T, Sigrist SJ (2018). Coupling the structural and functional assembly of synaptic release sites. Front Neuroanat 12, 81.

Gimber N, Tadeus G, Maritzen T, Schmoranzer J, Haucke V (2015). Diffusional spread and confinement of newly exocytosed synaptic vesicle proteins. Nat Commun 6, 8392.

Goel P, Dufour Bergeron D, Böhme MA, Nunnelly L, Lehmann M, Buser C, Walter AM, Sigrist SJ, Dickman D (2019). Homeostatic scaling of active zone scaffolds maintains global synaptic strength. J Cell Biol 218, 1706–1724.

González-Gaitán M, Jäckle H (1997). Role of Drosophila alpha-adaptin in presynaptic vesicle recycling. Cell 88, 767–776.

Gratz SJ, Goel P, Bruckner JJ, Hernandez RX, Khateeb K, Macleod GT, Dickman D, O'Connor-Giles KM (2019). Endogenous tagging reveals differential regulation of Ca2+ channels at single active zones during presynaptic homeostatic potentiation and depression. J Neurosci 39, 2416–2429.

Gray EG, Pease HL (1971). On understanding the organisation of the retinal receptor synapses. Brain Res 35, 1–15.

Haralick RM, Shanmugam K, Dinstein I (1973). Textural features for image classification. IEEE Trans Syst Man Cybern SMC-3, 610–621.

Heerssen H, Fetter RD, Davis GW (2008). Clathrin dependence of synaptic-vesicle formation at the Drosophila neuromuscular junction. Curr Biol 18, 401–409.

Henne WM, Boucrot E, Meinecke M, Evergren E, Vallis Y, Mittal R, McMahon HT (2010). FCHo proteins are nucleators of clathrin-mediated endocytosis. Science 328, 1281–1284.

Heuser JE, Reese TS (1973). Evidence for recycling of synaptic vesicle membrane during transmitter release at the frog neuromuscular junction. J Cell Biol 57, 315–344.

Hong H, Zhao K, Huang S, Huang S, Yao A, Jiang Y, Sigrist S, Zhao L, Zhang YQ (2020). Structural remodeling of active zones is associated with synaptic homeostasis. J Neurosci 40, 2817–2827.

Honigmann A, van den Bogaart G, Iraheta E, Risselada HJ, Milovanovic D, Mueller V, Müllar S, Diederichsen U, Fasshauer D, Grubmüller H, et al. (2013). Phosphatidylinositol 4,5-bisphosphate clusters act as molecular beacons for vesicle recruitment. Nat Struct Mol Biol 20, 679–686.

Hosoi N, Holt M, Sakaba T (2009). Calcium Dependence of exo- and endocytotic coupling at a glutamatergic synapse. Neuron 63, 216–229.

Hua Y, Woehler A, Kahms M, Haucke V, Neher E, Klingauf J (2013). Blocking endocytosis enhances short-term synaptic depression under conditions of normal availability of vesicles. Neuron 80, 343–349.

Imoto Y, Raychaudhuri S, Ma Y, Fenske P, Sandoval E, Itoh K, Blumrich E-M, Matsubayashi HT, Mamer L, Zarebidaki F, et al. (2022). Dynamin is primed at endocytic sites for ultrafast endocytosis. Neuron 110, 2815–2835.e13.

Jang S, Lee H, Kim E (2017). Synaptic adhesion molecules and excitatory synaptic transmission. Curr Opin Neurobiol Mol Neurosci 45, 45–50.

Jäpel M, Gerth F, Sakaba T, Bacetic J, Yao L, Koo S-J, Maritzen T, Freund C, Haucke V (2020). Intersectin-mediated clearance of SNARE complexes is required for fast neurotransmission. Cell Rep 30, 409–420.e6.

Jiao W, Andrey S, Oleg S (2010). A semi-correlative technique for the subcellular localization of proteins in Drosophila synapses. J Neurosci Methods 185, 273–279.

Jorgensen EM, Hartwieg E, Schuske K, Nonet ML, Jin Y, Horvitz HR (1995). Defective recycling of synaptic vesicles in synaptotagmin mutants of Caenorhabditis elegans. Nature 378, 196–199.

Kaksonen M, Roux A (2018). Mechanisms of clathrin-mediated endocytosis. Nat Rev Mol Cell Biol 19, 313–326.

Kasprowicz J, Kuenen S, Miskiewicz K, Habets RLP, Smitz L, Verstreken P (2008). Inactivation of clathrin heavy chain inhibits synaptic recycling but allows bulk membrane uptake. J Cell Biol 182, 1007–1016.

Kawasaki F, Hazen M, Ordway RW (2000). Fast synaptic fatigue in shibire mutants reveals a rapid requirement for dynamin in synaptic vesicle membrane trafficking. Nat Neurosci 3, 859.

Kawasaki F, Iyer J, Posey LL, Sun CE, Mammen SE, Yan H, Ordway RW (2011). The DISABLED protein functions in CLATHRIN-mediated synaptic vesicle endocytosis and exoendocytic coupling at the active zone. Proc Natl Acad Sci USA 108, E222–E229.

Kelley CF, Messelaar EM, Eskin TL, Wang S, Song K, Vishnia K, Becalska AN, Shupliakov O, Hagan MF, Danino D, et al. (2015). Membrane charge directs the outcome of F-BAR domain lipid binding and autoregulation. Cell Rep 13, 2597–2609.

Khuong TM, Habets RLP, Kuenen S, Witkowska A, Kasprowicz J, Swerts J, Jahn R, van den Bogaart G, Verstreken P (2013). Synaptic PI(3,4,5)P3 is required for Syntaxin1A clustering and neurotransmitter release. Neuron 77, 1097–1108.

Khuong TM, Habets RLP, Slabbaert JR, Verstreken P (2010). WASP is activated by phosphatidylinositol-4,5-bisphosphate to restrict synapse growth in a pathway parallel to bone morphogenetic protein signaling. Proc Natl Acad Sci USA 107, 17379–17384.

Kidokoro Y 2006. Vesicle trafficking and recycling at the neuromuscular junction: two pathways for endocytosis. Int Rev Neurobiol 75, 145–164.

Kittel RJ, Wichmann C, Rasse TM, Fouquet W, Schmidt M, Schmid A, Wagh DA, Pawlu C, Kellner RR, Willig KI, et al. (2006). Bruchpilot promotes active zone assembly, Ca2+ channel clustering, and vesicle release. Science 312, 1051–1054.

Koenig JH, Ikeda K (1996). Synaptic vesicles have two distinct recycling pathways. J Cell Biol 135, 797–808.

Koh T-W, Verstreken P, Bellen HJ (2004). Dap160/intersectin acts as a stabilizing scaffold required for synaptic development and vesicle endocytosis. Neuron 43, 193–205.

Koles K, Yeh AR, Rodal AA (2015). Tissue-specific tagging of endogenous loci in Drosophila melanogaster. Biol Open 5, 83–89.

Kosaka T, Ikeda K (1983). Possible temperature-dependent blockage of synaptic vesicle recycling induced by a single gene mutation in drosophila. J Neurobiol 14, 207–225.

Kondo S, Ueda R (2013). Highly improved gene targeting by germline-specific Cas9 expression in Drosophila. Genetics 195, 715–721.

Kozak M, Kaksonen M (2022). Condensation of Ede1 promotes the initiation of endocytosis. eLife 11, e72865.

Kuromi H, Ueno K, Kidokoro Y (2010). Two types of Ca2+ channel linked to two endocytic pathways coordinately maintain synaptic transmission at the Drosophila synapse. Eur J Neurosci 32, 335–346.

Kurshan PT, Merrill SA, Dong Y, Ding C, Hammarlund M, Bai J, Jorgensen EM, Shen K (2018). γ-Neurexin and Frizzled mediate parallel synapse assembly pathways antagonized by receptor endocytosis. Neuron 100, 150–166.e4.

Legland D, Arganda-Carreras I, Andrey P (2016). MorphoLibJ: integrated library and plugins for mathematical morphology with ImageJ. Bioinformatics 32, 3532–3534.

Leshchyns'ka I, Sytnyk V, Richter M, Andreyeva A, Puchkov D, Schachner M (2006). The adhesion molecule CHL1 regulates uncoating of clathrin-coated synaptic vesicles. Neuron 52, 1011–1025.

Li C, Tam P (1998). An iterative algorithm for minimum cross entropy thresholding. Pattern Recognit Lett 19, 771–776.

Li T-N, Chen Y-J, Lu T-Y, Wang Y-T, Lin H-C, Yao C-K (2020). A positive feedback loop between Flower and PI(4,5)P2 at periactive zones controls bulk endocytosis in Drosophila. eLife 9, e60125.

Littleton JT, Bai J, Vyas B, Desai R, Baltus AE, Garment MB, Carlson SD, Ganetzky B, Chapman ER (2001). Synaptotagmin mutants reveal essential functions for the C2B domain in Ca2+-triggered fusion and recycling of synaptic vesicles in vivo. J Neurosci 21, 1421–1433.

Luo JK, Melland H, Nithiananantharajah J, Gordon SL (2021). Postsynaptic Neuroligin-1 mediates presynaptic endocytosis during neuronal activity. Front Mol Neurosci 14, 744845.

Marie B, Sweeney ST, Poskanzer KE, Roos J, Kelly RB, Davis GW (2004). Dap160/intersectin scaffolds the periactive zone to achieve high-fidelity endocytosis and normal synaptic growth. Neuron 43, 207–219.

Maritzen T, Haucke V (2018). Coupling of exocytosis and endocytosis at the presynaptic active zone. Neurosci Res 127, 45–52.

Matkovic T, Siebert M, Knoche E, Depner H, Mertel S, Owald D, Schmidt M, Thomas U, Sickmann A, Kamin D, et al. (2013). The Bruchpilot cytomatrix determines the size of the readily releasable pool of synaptic vesicles. J Cell Biol 202, 667–683.

Melom JE, Akbergenova Y, Gavornik JP, Littleton JT (2013). Spontaneous and evoked release are independently regulated at individual active zones. J Neurosci 33, 17253–17263.

Nahm M, Park S, Lee J, Lee S (2016). MICAL-like regulates Fasciclin II membrane cycling and synaptic development. Mol Cells 39, 762–767.

Neher E (2010). What is rate-limiting during sustained synaptic activity: vesicle supply or the availability of release sites. Front Synaptic Neurosci 2, 144.

Newman ZL, Bakshinskaya D, Schultz R, Kenny SJ, Moon S, Aghi K, Stanley C, Marnani N, Li R, Bleier J, et al. (2022). Determinants of synapse diversity revealed by super-resolution quantal transmission and active zone imaging. Nat Commun 13, 229.

Nicholson-Tomishima K, Ryan TA (2004). Kinetic efficiency of endocytosis at mammalian CNS synapses requires synaptotagmin I. Proc Natl Acad Sci USA 101, 16648–16652.

O'Connor-Giles KM, Ho LL, Ganetzky B (2008). Nervous Wreck interacts with Thickveins and the endocytic machinery to attenuate retrograde BMP signaling during synaptic growth. Neuron 58, 507–518.

Petzoldt AG, Lützkendorf J, Sigrist SJ (2016). Mechanisms controlling assembly and plasticity of presynaptic active zone scaffolds. Curr Opin Neurobiol 39, 69–76.

Poskanzer KE, Fetter RD, Davis GW (2006). Discrete residues in the c(2)b domain of synaptotagmin I independently specify endocytic rate and synaptic vesicle size. Neuron 50, 49–62.

Poskanzer KE, Marek KW, Sweeney ST, Davis GW (2003). Synaptotagmin I is necessary for compensatory synaptic vesicle endocytosis in vivo. Nature 426, 559–563.

Posor Y, Eichhorn-Gruenig M, Puchkov D, Schöneberg J, Ullrich A, Lampe A, Müller R, Zarbakhsh S, Gulluni F, Hirsch E, et al. (2013). Spatiotemporal control of endocytosis by phosphatidylinositol-3,4-bisphosphate. Nature 499, 233–237.

Ramachandran P, Budnik V (2010). Electron microscopy of Drosophila larval neuromuscular junctions. Cold Spring Harb Protoc 2010, pdb. prot5474.

Reshetniak S, Ußling J-E, Perego E, Rammner B, Schikorski T, Fornasiero EF, Truckenbrodt S, Köster S, Rizzoli SO (2020). A comparative analysis of the mobility of 45 proteins in the synaptic bouton. EMBO J 39, e104596.

Rodal AA, Blunk AD, Akbergenova Y, Jorquera RA, Buhl LK, Littleton JT (2011). A presynaptic endosomal trafficking pathway controls synaptic growth signaling. J Cell Biol 193, 201–217.

Rodal AA, Motola-Barnes RN, Littleton JT (2008). Nervous wreck and Cdc42 cooperate to regulate endocytic actin assembly during synaptic growth. J Neurosci 28, 8316–8325.

Roos J, Kelly RB (1998). Dap160, a neural-specific Eps15 homology and multiple SH3 domain-containing protein that interacts with Drosophila dynamin. J Biol Chem 273, 19108–19119.

Roos J, Kelly RB (1999). The endocytic machinery in nerve terminals surrounds sites of exocytosis. Curr Biol 9, 1411–1414.

Sakaba T, Kononenko NL, Bacetic J, Pechstein A, Schmoranzer J, Yao L, Barth H, Shupliakov O, Kobler O, Aktories K, Haucke V (2013). Fast neurotransmitter release regulated by the endocytic scaffold intersectin. Proc Natl Acad Sci USA 110, 8266–8271.

Schuster CM, Davis GW, Fetter RD, Goodman CS (1996). Genetic dissection of structural and functional components of synaptic plasticity. I. Fasciclin II controls synaptic stabilization and growth. Neuron 17, 641–654.

Shetty A, Sytnyk V, Leshchyns'ka I, Puchkov D, Haucke V, Schachner M (2013). The neural cell adhesion molecule promotes maturation of the presynaptic endocytotic machinery by switching synaptic vesicle recycling from adaptor protein 3 (AP-3)- to AP-2-dependent mechanisms. J Neurosci 33, 16828–16845.

Shupliakov O, Bloom O, Gustafsson JS, Kjaerulff O, Low P, Tomilin N, Pieribone VA, Greengard P, Brodin L (2002). Impaired recycling of synaptic vesicles after acute perturbation of the presynaptic actin cytoskeleton. Proc Natl Acad Sci USA 99, 14476–14481.

Sone M, Suzuki E, Hoshino M, Hou D, Kuromi H, Fukata M, Kuroda S, Kaibuchi K, Nabeshima Y, Hama C (2000). Synaptic development is controlled in the periactive zones of Drosophila synapses. Development 127, 4157–4168.

Stanishneva-Konovalova TB, Kelley CF, Eskin TL, Messelaar EM, Wasserman SA, Sokolova OS, Rodal AA (2016). Coordinated autoinhibition of F-BAR domain membrane binding and WASp activation by Nervous Wreck. Proc Natl Acad Sci USA 113, E5552–E5561.

Südhof TC (2018). Towards an understanding of synapse formation. Neuron 100, 276–293.

Sytnyk V, Leshchyns'ka I, Schachner M (2017). Neural cell adhesion molecules of the immunoglobulin superfamily regulate synapse formation, maintenance, and function. Trends Neurosci 40, 295–308.

Teng H, Wilkinson RS (2000). Clathrin-mediated endocytosis near active zones in snake motor boutons. J Neurosci 20, 7986–7993.

van Stegen B, Dagar S, Gottmann K (2017). Release activity-dependent control of vesicle endocytosis by the synaptic adhesion molecule N-cadherin. Sci Rep 7, 40865.

Verstreken P, Koh T-W, Schulze KL, Zhai RG, Hiesinger PR, Zhou Y, Mehta SQ, Cao Y, Roos J, Bellen HJ (2003). Synaptojanin is recruited by endophilin to promote synaptic vesicle uncoating. Neuron 40, 733–748.

Verstreken P, Ohyama T, Bellen HJ (2008). FM 1-43 labeling of synaptic vesicle pools at the Drosophila neuromuscular junction. Methods Mol Biol 440, 349–369.

Wagh DA, Rasse TM, Asan E, Hofbauer A, Schwenkert I, Durrbeck H, Buchner S, Dabauvalle M-C, Schmidt M, Qin G, et al. (2006). Bruchpilot, a protein with homology to ELKS/CAST, is required for structural integrity and function of synaptic active zones in Drosophila. Neuron 49, 833–844.

Wahl S, Katiyar R, Schmitz F (2013). A local, periactive zone endocytic machinery at photoreceptor synapses in close vicinity to synaptic ribbons. J Neurosci 33, 10278–10300.

Wahl S, Magupalli VG, Dembla M, Katiyar R, Schwarz K, Köblitz L, Alpadi K, Krause E, Rettig J, Sung C-H, et al. (2016). The disease protein Tulp1 is essential for periactive zone endocytosis in photoreceptor ribbon synapses. J Neurosci 36, 2473–2493.

Walter AM, Müller R, Tawfik B, Wierda KD, Pinheiro PS, Nadler A, McCarthy AW, Ziomkiewicz I, Kruse M, Reither G, et al. (2017). Phosphatidylinositol 4,5-bisphosphate optical uncaging potentiates exocytosis. eLife 6, e30203.

Wan HI, DiAntonio A, Fetter RD, Bergstrom K, Strauss R, Goodman CS (2000). Highwire regulates synaptic growth in Drosophila. Neuron 26, 313–329.

Watanabe S, Liu Q, Davis MW, Hollopeter G, Thomas N, Jorgensen NB, Jorgensen EM (2013a). Ultrafast endocytosis at Caenorhabditis elegans neuromuscular junctions. eLife 2, e00723.

Watanabe S, Rost BR, Camacho-Pérez M, Davis MW, Söhl-Kielczynski B, Rosenmund C, Jorgensen EM (2013b). Ultrafast endocytosis at mouse hippocampal synapses. Nature 504, 242–247.

Weyhersmüller A, Hallermann S, Wagner N, Eilers J (2011). Rapid active zone remodeling during synaptic plasticity. J Neurosci 31, 6041–6052.

Wilhelm BG, Mandad S, Truckenbrodt S, Kröhnert K, Schäfer C, Rammner B, Koo SJ, Claßen GA, Krauss M, Haucke V, et al. (2014). Composition of isolated synaptic boutons reveals the amounts of vesicle trafficking proteins. Science 344, 1023–1028.

Winther ÅME, Jiao W, Vorontsova O, Rees KA, Koh T-W, Sopova E, Schulze KL, Bellen HJ, Shupliakov O (2013). The dynamin-binding domains of Dap160/intersectin affect bulk membrane retrieval in synapses. J Cell Sci 126, 1021–1031.

Winther ÅME, Vorontsova O, Rees KA, Näreoja T, Sopova E, Jiao W, Shupliakov O (2015). An endocytic scaffolding protein together with synapsin regulates synaptic vesicle clustering in the Drosophila neuromuscular junction. J Neurosci 35, 14756–14770.

Wood KM, Smith CJ (2021). Clathrin: the molecular shape shifter. Biochem J 478, 3099–3123.

Wu L-G, Hamid E, Shin W, Chiang H-C (2014). Exocytosis and endocytosis: modes, functions, and coupling mechanisms. Annu Rev Physiol 76, 301–331.

Wu X-S, McNeil BD, Xu J, Fan J, Xue L, Melicoff E, Adachi R, Bai L, Wu L-G (2009). Ca2+ and calmodulin initiate all forms of endocytosis during depolarization at a nerve terminal. Nat Neurosci 12, 1003–1010.

Yamada M, Hashimoto T, Hayashi N, Higuchi M, Murakami A, Nakashima T, Maekawa S, Miyata S (2007). Synaptic adhesion molecule OBCAM; synaptogenesis and dynamic internalization. Brain Res 1165, 5–14.

Yao J, Kwon SE, Gaffaney JD, Dunning FM, Chapman ER (2011). Uncoupling the roles of synaptotagmin I during endo- and exocytosis of synaptic vesicles. Nat Neurosci 15, 243–249.